Surface & Coatings Technology 506 (2025) 132094

Contents lists available at ScienceDirect

Surface & Coatings Technology

journal homepage: www.elsevier.com/locate/surfcoat

Cerium-containing hexamethyldisiloxane coatings for corrosion protection of a laser-based powder bed fusion fabricated AlSi10Mg0.3 alloy☆

Mirjam Spuller [a,*], Nina Kovač [b,c], Peter Rodič [b], Lukasz Major [d], Simon Chwatal [a], Mattia Cabrioli [e], Matteo Vanazzi [e], Giorgio De Pasquale [f], Juergen M. Lackner [a], Reinhard Kaindl [a], Wolfgang Waldhauser [a]

[a] Joanneum Research Forschungsgesellschaft mbH, Materials – Institute for Sensors, Photonics and Manufacturing Technologies, Leobner Str. 94a, A-8712 Niklasdorf, Austria
[b] Jožef Stefan Institute, Department of Physical and Organic Chemistry, Jamova c. 39, SI-1000 Ljubljana, Slovenia
[c] Jožef Stefan International Postgraduate School, SI-1000 Ljubljana, Slovenia
[d] Polish Academy of Sciences, Institute of Metallurgy and Materials Science, Władysława Reymonta 25, 30-059 Kraków, Poland
[e] f3nice, Via Roccoli 252, I-23010 Piantedo, Italy
[f] Politecnico di Torino, Smart Structures and Systems Lab, Corso Duca degli Abruzzi 24, I-10129 Torino, Italy

ARTICLE INFO

Keywords:
AlSi10Mg0.3
Atmospheric pressure plasma deposition (APPD)
Hexamethyldisiloxane
Corrosion protective coating
Cerium salts
Laser-based powder bed fusion
Cerium oxide nanoparticles

ABSTRACT

This study investigates the formation and mechanism of action of advanced cerium-containing hexamethyldisiloxane (HMDSO) coatings to improve the corrosion resistance of AlSi10Mg0.3 alloy, fabricated by laser-based powder bed fusion (L-PBF). HMDSO coatings were deposited using an aerosol-assisted atmospheric pressure plasma deposition (APPD) process to protect the metal surface. This study investigated the effect of different cerium concentrations in the aerosol solution on the deposition process.

The coatings were characterised using profilometry to determine coating thickness, while light optical microscopy was used for morphology analyses. Fourier transform infrared spectroscopy and transmission electron microscopy provided detailed information about coating formation and microstructure, while corrosion behaviour was assessed through potentiodynamic polarisation (PDP) measurements in 0.1 M NaCl solution and six-weeks salt-spray tests (ASTM B117–23).

Results showed that aerosol-assisted APPD enables the deposition of approximately 800 nm thick HMDSO coatings with incorporated CeO_2 nanoparticles. Corrosion measurements revealed reduced corrosion current density, indicating improved corrosion resistance. The presence of cerium in the coatings further enhanced this resistance, as the formed CeO_2 nanoparticles acted as diffusion barriers against the corrosive medium. Corrosion testing confirmed that the coating with 10 wt% cerium in the aerosol solution provided the most durable protection. Cerium-containing HMDSO coatings have demonstrated beneficial corrosion protection for L-PBF-fabricated AlSi10Mg0.3 with further possible improvements in studying active protection.

1. Introduction

Aluminium alloys are fundamental to modern engineering, and they have found extensive applications in the automotive and aerospace industries due to their exceptional strength-to-weight ratio. This key property enhances fuel efficiency and overall performance and reduces emissions and costs [1]. Traditionally, aluminium components have been produced using conventional manufacturing processes such as casting or machining, but these methods often limit design flexibility and material efficiency [2]. In contrast, laser-based powder bed fusion (L-PBF), an advanced additive manufacturing technique, has emerged as a transformative process for aluminium alloys [3,4]. L-PBF allows for the precise fabrication of complex and lightweight components, making it particularly attractive for aerospace and high-performance applications [3,5].

Compared to conventionally manufactured aluminium alloys, L-PBF-

☆ This article is part of a Special issue entitled: 'PSE 2024' published in Surface & Coatings Technology.

* Corresponding author.
E-mail address: mirjam.spuller@joanneum.at (M. Spuller).

https://doi.org/10.1016/j.surfcoat.2025.132094
Received 31 December 2024; Received in revised form 9 March 2025; Accepted 26 March 2025
Available online 28 March 2025

fabricated ones offer several advantages [5–7]. These include enhanced geometric freedom, reduced material waste, and the ability to tailor microstructures to achieve specific mechanical properties [8,9]. One of L-PBF's most commonly used aluminium alloys is the near-eutectic AlSi10Mg0.3 alloy, which exhibits favourable melting behaviour due to its low melting point and reduced susceptibility to hot cracking [9]. Rapid solidification during L-PBF enables the formation of refined microstructures, which contributes to superior mechanical properties, such as higher or at least comparable hardness and strength, when compared to conventionally manufactured AlSi10Mg0.3 [8–11]. However, despite these benefits, L-PBF-fabricated AlSi10Mg0.3 is particularly susceptible to corrosion, especially in harsh or chloride-rich environments [5,12,13].

A key challenge in utilising L-PBF-fabricated AlSi10Mg0.3 is its susceptibility to corrosion, driven by unique microstructural features [7,12,13]. The laser melting process creates microstructural heterogeneities, including melting pools and the formation of a fine eutectic microstructure composed of α-Al and Si phases, which serve as preferential sites for localised corrosion [9,13]. Moreover, post-fabrication solution heat treatments, necessary to optimise mechanical properties [9,13,14], can further exacerbate the alloy's susceptibility to corrosion [14,15]. These challenges are compounded by the growing environmental regulations that restrict the use of hazardous substances, such as hexavalent chromium (Cr(VI)), a commonly used corrosion inhibitor in traditional coating systems [16–18]. Cr(VI) compounds are highly effective in providing corrosion resistance but are toxic and carcinogenic [19,20], driving the need for safer alternatives [21].

Traditional coating systems, which often rely on additive or spray-based methods, are not entirely suitable for L-PBF alloys due to their reliance on thicker coatings and lack of compatibility with the microstructure of L-PBF-fabricated parts. These coatings may fail to adequately adhere to the complex surface features of L-PBF components or prevent the localised corrosion initiated by microstructural defects. As a result, there is an urgent need to develop advanced coating systems tailored to the specific requirements of L-PBF aluminium alloys [22].

State-of-the-art approaches to corrosion protection of aluminium alloys focus on developing environmentally friendly solutions that combine passive and active protection mechanisms [5,22]. Various surface treatments and coating methods have been proposed and studied, including plasma electrolytic oxidation, micro-arc oxidation process, CVD, PVD, and sol-gel coating [23–29]. Among these methods, sol-gel coating gained much attention due to its simple fabrication route, cost efficiency, and adaptability, while offering good corrosion resistance. Zhou et al. [30] demonstrated that benzoxazine-based hybrid sol-gel coating (TEOS-PBz), applied by dip-coating, provides improved protection against corrosion, if a fully developed cross-linked network structure and highly water-repellent polymer matrix is achieved by an optimised curing procedure. A study of Li et al. [31] deals with the sol-bath-gel approach including dipping of the aluminium alloy into silane sol, slowly withdrawing, and drying. Potentiodynamic polarisation and electrochemical impedance testing of the prepared hybrid coating confirmed its ability to suppress the anodic dissolution, providing long-term corrosion protection, which can be greater than that of the chromate conversion coating. Furthermore, Jafari-Tarzanagh et al. [32] reported enhanced corrosion protection of AA2024 by incorporating diclofenac sodium-loaded (DFS) Santa Barbara Amorphous-15 (SBA-15) silica into the sol-gel coating. They show that the polarisation resistance over 150 days in simulated acid rain significantly increases from 0.006 to 0.05 MΩ cm^2 after incorporating aminated SBA-15 and can be further increased to 14.454 MΩ cm^2 when encapsulated DFS-loaded SBA-15 was added into the coating, demonstrating the active corrosion protection.

Nevertheless, another promising alternative to deposit environmentally friendly polysiloxane coatings is atmospheric pressure plasma deposition (APPD) [33–35]. Although APPD requires special equipment, such as a plasma jet, and demands significant effort for process optimisation [36], it offers several advantages over other commonly used methods. For example, coating deposition using APPD can take place in a single-step deposition, without time- and energy-consuming drying, or curing processes, as often required in the sol-gel method, to get cross-linked and dense coatings. Additionally, critical issues such as the material waste due to contamination of the liquid sol-gel bath are absent in the APPD process. APPD combines the advantage of precisely controlled deposition of the desired coating thickness even for complex three-dimensional parts, how it is the case for the CVD and PVD process, with an order of magnitude larger possible deposition rates (up to 100 nm/s), which are of the order of magnitude suitable demanded by industrial applications [37]. However, compared to CVD and PVD, APPD eliminates the need for a vacuum chamber [38], making it a cost-effective and scalable process, with high potential for automation and continuous production [39]. In order to provide adequate corrosion protection, a well-adhering coating is essential. Using APPD, this can be easily achieved with a plasma pretreatment of the samples' surface using argon gas directly before depositing the coating without further handling of the sample [40,41].

To realise an environmentally friendly coating using APPD, hexamethyldisiloxane (HMDSO) is a commonly used organosilicon precursor [42]. The monomer HMDSO has gained significant interest in the APPD method due to its flexibility in the backbone's Si–O–Si bond and the water-repellence of its formed polysiloxane coatings.

As already reported in [33,43], plasma-polymerised HMDSO coatings demonstrate good corrosion protection on various aluminium alloys. However, due to porosity inside the coatings' cross-linked network, water permeates through the coating, reducing the corrosion resistance over time [44].

To optimise the long-term corrosion protection, cerium-based compounds using as corrosion inhibitors, gained attention. The compounds have especially garnered attention as corrosion inhibitors due to their environmentally benign nature and multifunctional protective properties [45–48]. Cerium incorporated into coatings enhances corrosion resistance through two primary mechanisms: (i) passive barrier protection and (ii) active inhibition or self-healing [48–50]. Passive barrier coatings form a physical barrier to isolate the substrate from the corrosive environment, while active inhibition occurs when cerium ions (Ce^{3+}) respond to localised damage [51–55]. The formation of hydroxide ions (OH^-) at the damaged sites triggers the precipitation of cerium hydroxide ($Ce(OH)_3$), which subsequently oxidises into cerium oxide (CeO_2), effectively sealing the defect [46–48,56].

With APPD, the deposition of doped coatings through an aerosol-assisted deposition mode is possible, allowing precise control over the coating composition [57,58]. In this deposition mode, salts can be introduced into the plasma via water-based solutions, modifying coating properties and enhancing the corrosion resistance [9].

This study aims to fill a critical gap in addressing the corrosion challenges of L-PBF-fabricated AlSi10Mg0.3 by developing cerium-containing HMDSO coatings using aerosol-assisted APPD. Coatings produced with HMDSO, as a precursor, along with a cerium-containing aerosol were deposited onto aluminium substrates. Coating characterisation was conducted using profilometry, light optical and transmission electron microscopy, and Fourier transform infrared spectroscopy. Corrosion resistance, in particular the passive barrier protection, was evaluated in 0.1 M NaCl solution by using potendiodynamic polarisation measurements and salt-spray chamber tests, to gain an in-depth knowledge of these coatings. The findings reveal their potential as innovative, environmentally friendly, and effective passive corrosion protection solutions, with the potential to transform automotive and aerospace applications.

2. Materials and methods

2.1. Chemicals and material

L-PBF-fabricated AlSi10Mg0.3 alloy plates with dimensions of 100 ×

70 × 3 mm^3 produced by f3Nice, Piantedo, Italy, were used as substrates. For coating deposition, the precursor HMDSO ≥98 % and cerium (III) nitrate hexahydrate ($Ce(NO_3)_3$ × 6 H_2O, 99 % trace metals basis), both from Merck Chemicals and Life Science GesmbH, Vienna, Austria, were used. The corrosive medium, 0.1 M NaCl solution, was prepared with NaCl (purity >99.5 %, AppliChem, Germany) and Milli-Q Direct water with a resistivity of 18.2 M cm^2 at 25 °C (Millipore, Billerica, MA).

Silicon (Si) wafer pieces (p-type, boron-doped, Active Business Company GmbH, Germany) were placed on the platform next to the AlSi10Mg0.3 substrates for additional coating characterisation. A small heat-resistant polyimide (Kapton®) tape was used to fix the Si wafer pieces beneath the moveable plasma source, and it also served as a mask for further coating thickness measurements.

2.2. Sample preparation

2.2.1. Grinding and cleaning

The mechanical grinding of the sample surface was performed using the Struers Tegramin 30 machine. First, a MD Molto plate was used for grinding (contact pressure: 300 N, rotation speed: 40 rpm, time: 1 min). The second step involved using a SiC paper with a grit P1200, applying a contact pressure of 300 N, a rotation speed of 40 rpm, and a duration of 1 min. All grinding steps were performed in the presence of water. Afterwards, all AlSi10Mg0.3 substrates were ultrasonically cleaned in ethanol for 5 min. Samples were dried in the air for at least 30 min.

2.2.2. Coatings deposition

An aerosol-assisted APPD setup was used to deposit the coatings (Fig. 1 and Figure S1). The hot gas plasma source (Type: IC3, INOCON Technologie GmbH, Austria) was operated with argon as a plasma gas with a flow rate of 10 L/min. The ground AlSi10Mg0.3 substrates were

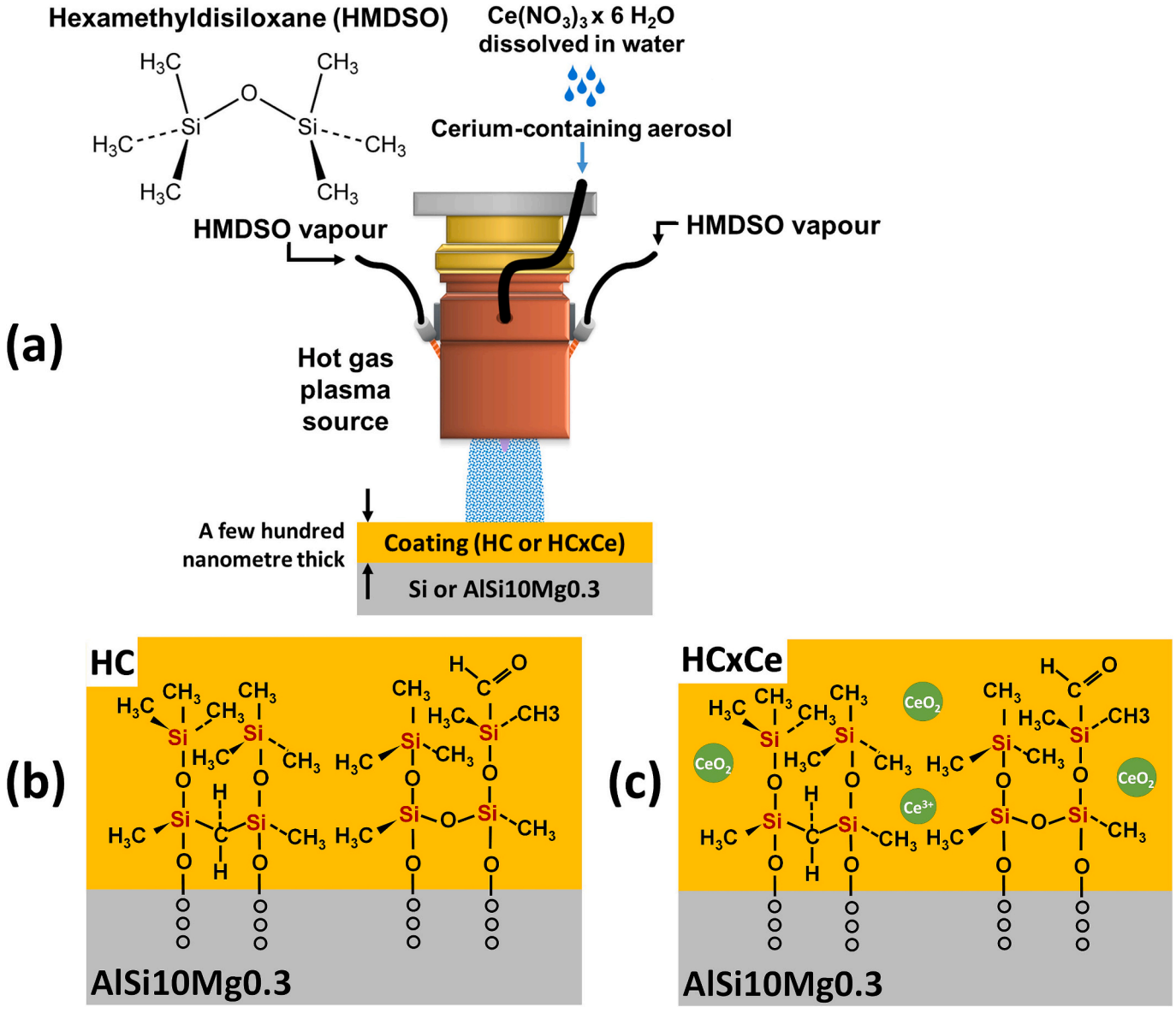

Fig. 1. (a) Schematic representation of the aerosol-assisted atmospheric pressure plasma deposition (APPD) setup. HMDSO was used as a precursor for the coating process. It was combined with an aerosol generated from a cerium nitrate hexahydrate solution ($Ce(NO_3)_3$ x 6 H_2O dissolved in H_2O) in the plasma. The plasma source directs the reactive plasma onto the substrate for coating deposition to produce a few hundred nm thick coating. (b) Schematic representation of the coating structure formed by polymerisation of HMDSO without and (c) with addition of an aerosol in the plasma process. In this study, various solutions for aerosolisation were used, containing different concentrations of cerium (x = 5, 10, 15, and 20 wt%).

fixed on the platform with double-sided tape for the deposition. Next to the substrates the Si wafer pieces were placed. Before the coating process, all substrates were plasma pre-treated (100 A, 100 mm/s, 2 runs) to remove organic contaminants from the samples' surface.

As a precursor, evaporated HMDSO with a 50 mL/min flow rate was used (dosing system Sura Instruments STS 10.2, Germany). The HMDSO vapour was introduced via external feeds into the plasma (Fig. 1a). Compressed air was used as a carrier gas for the precursor (6 bar).

Cerium nitrate hexahydrate, ($Ce(NO_3)_3 \times 6\ H_2O$), was dissolved in distilled water by stirring for 5 min. For this study, solutions with varying cerium concentration from 5 up to 20 weight percentage (wt%) were prepared (Table 1). For coating deposition, the solution with the specific concentration was filled into an aerosol generator vessel (ATM211, Topas GmbH, Germany). Compressed air, at an inlet pressure of 6 bar, was used as the carrier gas for the aerosol. Its pressure was manually set to 0.75 bar using a pressure regulator on the aerosol generator, corresponding to an air flow rate of 14 L/min. The aerosol generator utilises a two-substance nozzle with a nozzle diameter of 1.1 mm to aerosolise the cerium-containing solution. This aerosol was simultaneously introduced into the plasma at a flow rate of 0.0167 mL/min (≙ 0.0033 g/min of cerium for the 20 wt% aerosol) via internal feeds, along with HMDSO vapour introduced via external feeds (Fig. 1a). This results in an HMDSO-to-aerosol ratio of 2989:1 in the plasma.

The plasma was operated with a discharge current of 120 A. To achieve a homogeneous coating, the path of the plasma jet was a meander with a speed of 100 mm/s 50 mm above the substrate. After each complete pass, the meander was offset ±5 mm, resulting in multiple coating layers.

2.2.3. Coating variations

Coatings were produced on the L-PBF-AlSi10Mg0.3 substrate with the same (three) number of layers. In Table 1, the different variations of the produced samples are listed. Besides the uncoated reference, coatings were deposited with HMDSO and cerium-containing aerosols with concentrations ranging from 0, corresponding to no aerosol usage, up to 20 wt% in the aerosol. The sample abbreviation consists of the first letter of the precursor (H), coating (C) and amount of cerium in the aerosol (x = 5, 10, 15, 20 wt% Ce).

2.3. Coating characterisation and corrosion testing

2.3.1. Analysis of coating thickness and optical appearance

Coating characterisation included thickness measurements and light optical microscope analyses. Thickness measurements were carried out with a tactile profilometer (Veeco Dektak 150) on the simultaneously coated Si wafer pieces (30 × 30 mm^2), which were masked during the coating process. Light optical microscope analyses were performed on simultaneously coated Si wafer pieces to investigate the appearance of the coatings. Since a significant portion of the provided cerium is expected to undergo oxidation during the APPD process, as supported by literature [59,60], and cerium is incorporated in the HMDSO coating not only in the metallic state, the wt% of cerium differs from the cerium concentration of the solution used for aerosolisation. Therefore, to estimate the approximate concentration of cerium incorporated as cerium oxide in the coating, the standard test method for determining volume fraction by systematic manual point count, described in ASTM E562–02 [61], were applied on images (1138 pixel × 1138 pixel, 37.8 pixel/cm) of samples taken with a 100 x magnification. A point distance of 1 mm was chosen for the grid of points on the image, resulting in a total of 1681 points (P_T). Points that fall within the particles were manually counted and the volume fraction was estimated with Eq. (1):

$$V_{CeO_2} = P_p = \frac{P_i}{P_T} \times 100 \quad (1)$$

The concentration of cerium in wt% was obtained through the mass quantities and the ratio of M_{Ce}/M_{CeO_2}, using the mass of CeO_2 particles (ρ = 7.22 g/cm^3) and the mass of the SiO_xCH_x matrix (ρ = 1.43 g/cm^3 [62,63]). The procedure was repeated on five different images of the sample to obtain statistical values.

2.3.2. Fourier transform infrared spectroscopy

Fourier transform infrared spectroscopy (FTIR) was employed to characterise the coating formation. Measurements were performed with a Shimadzu IRSpirit spectrophotometer in damped total internal reflection mode between 400 cm^{-1} and 4000 cm^{-1}. The spectra were analysed using Shimadzu LabSolutions IR software, with baseline correction and smoothing applied before display.

2.3.3. Transmission electron microscopy

Detailed microstructural characterisation of selected coatings deposited on AlSi10Mg0.3 substrates was conducted using transmission electron microscopy (TEM). Analyses were performed in bright-field mode (TEM BF), scanning transmission mode (STEM), and high-resolution mode (HRTEM). Phase identification was carried out via selected area electron diffraction (SAED) and HRTEM imaging, while the qualitative chemical composition was analysed using energy-dispersive X-ray spectroscopy (EDXS).

A high-resolution TEM (ThermoFisher THEMIS) equipped with a field emission gun (FEG) and operating at an accelerating voltage of 200 kV was employed. Thin foils were prepared using the focused ion beam (FIB) technique to ensure electron transparency. This exploration was performed with a DualBeam SCIOS II scanning microscope (ThermoFisher), combining an electron beam for imaging and an ion beam for precise foil cutting. The system also included an automated preparation feature with AutoTEM4 software.

2.3.4. Potentiodynamic polarisation measurements

Potentiodynamic polarisation (PDP) measurements were performed in freshly prepared 0.1 M NaCl solution used as a corrosive media. Measurements were conducted at room temperature in a press-fit corrosion cell (250 mL volume) using a standard cell with three-electrode setup (K0235 Flat Cell Kit, Ametek, Figure S3). The working electrode was an AlSi10Mg0.3 substrate with an exposed surface area of 1.0 cm^2. A carbon rod was used as the counter electrode, while a saturated Ag/AgCl electrode ($E = 0.197\ V$ vs. the standard hydrogen electrode) was the reference electrode. Measurements were carried out using an Autolab PGSTAT 204 M potentiostat/galvanostat (Metrohm Autolab, Utrecht, Netherlands) controlled by Nova 2.1 software.

Before measurements, the samples could stabilize for 1 h under open circuit conditions. The stabilized quasi-steady-state potential at the end of this period was defined as the open-circuit potential (E_{oc}). PDP measurements were then conducted at a potential scan rate of 1 mV/s,

Table 1
Sample abbreviations for various samples investigated within this study: Uncoated samples (UNC), with HMDSO coated samples but without adding a cerium-containing aerosol in the deposition process (HC), and with adding cerium-containing aerosols using different cerium concentrations; for 5 wt% HC5Ce, for 10 wt% HC10Ce, for 15 wt% HC15Ce, for 20 wt% HC20Ce.

Abbreviation	Coating deposition components		Flow rates of components	
	Components	Ce-concentration of aerosol [wt%]	HMDSO flow rate [mL/min]	Aerosol flow rate [mL/min]
UNC	–	–	–	–
HC	HMDSO	–	50	–
HC5Ce	HMDSO + aerosol	5	50	0.0167
HC10Ce	HMDSO + aerosol	10	50	0.0167
HC15Ce	HMDSO + aerosol	15	50	0.0167
HC20Ce	HMDSO + aerosol	20	50	0.0167

starting at −250 mV relative to E_{oc}. The potential increased anodically up to 1 V vs. Ag/AgCl. Each measurement was repeated thrice, and a representative dataset was selected.

Electrochemical corrosion parameters, including the corrosion current density (j_{corr}) and corrosion potential (E_{corr}), were determined from the polarisation curves using Tafel extrapolation. The coating breakdown potential (E_{bd}) was identified as the potential within the passive region where the current density increased sharply. ΔE was calculated as the absolute value of the difference between E_{bd} and E_{corr} ($\Delta E = |E_{bd} - E_{corr}|$).

2.3.5. Salt-spray chamber testing

In addition, accelerated corrosion tests were conducted on ground and coated AlSi10Mg0.3 samples. The edges and backside of the samples were masked with adhesive power tape, exposing a surface area of 100 × 70 mm^2 to the salt-spray environment. The tests were carried out in an HKT 750 BASIC-LINE salt-spray chamber (KÖHLER, 0.750 m^3 capacity) following the ASTM B117–23 standard.

The NaCl solution (50 ± 1 g/L) was prepared with an initial pH of 6.0–6.5 at room temperature and adjusted to a range of 6.5–7.2 at 35 °C. The pH was regulated using 0.1 M NaOH or HCl solutions. The spraying system included a clean air supply with controlled pressure and humidity, a reservoir for the salt solution, and a single nozzle sprayer. The chamber temperature was maintained at 35 ± 1 °C, and the spray rate was set to approximately 1 mL/h, verified using standardised collection devices (glass funnels and graduated cylinders).

The test duration was up to 6 weeks (~1000 h). After the test, samples were thoroughly rinsed with tap and distilled water to remove salt deposits and loose corrosion products. Photos of the samples were taken before the test, after 3 weeks and 6 weeks to facilitate qualitative analyses.

2.3.6. Analysis of corrosion attack

Quantitative photo analyses of the corrosion attacks were performed using ImageJ software. Representative image sections were selected and converted to 8-bit images. Individually defined thresholds were applied to distinguish corroded areas from protected regions using specific grey value ranges. These thresholded images were then used to calculate the percentage of the area affected by corrosion. The results were validated using a Python code (Figure S2). Each analysis was repeated three times per sample, and an average corrosion attack percentage was determined. Secondary electron (SE) micrographs of samples were taken before and after the salt-spray chamber test with a TESCAN VEGA3 microscope equipped with a heated tungsten filament and a 20 kV high-voltage supply. Additionally, chemical analyses using EDXS were performed with an Oxford detector at 20 kV over an area of 4.5 × 3.0 mm^2, in the same location as the before acquired SE micrographs. Surface element distributions, including aluminium, oxygen, carbon, silicon, sodium, chloride, and cerium, were normalised to 100 at.%.

3. Results and discussion

3.1. Thickness measurements

The thickness of HMDSO coatings on plasma-pretreated Si wafers increased by adding cerium nitrate, as illustrated in Fig. 2. The undoped HMDSO coating (HC) exhibited a thickness of 798 ± 29 nm, while adding cerium to higher concentrations increased the thickness, reaching a maximum of 938 ± 52 nm (HC20Ce). This trend is attributed to the influence of the cerium-containing aerosol introduced into the plasma. The aerosol introduces additional oxygen from the carrier gas into the plasma, enhancing coating formation and resulting in thicker coatings [64]. Additionally, it is suggested that the catalytic effect of cerium on the coating formation process [65] plays a significant role. The increased presence of cerium ions from the aerosol further influences the coating growth, resulting in thicker films. These observations highlight the critical role of the cerium nitrate solution in tuning the properties of HMDSO coatings for improved performance.

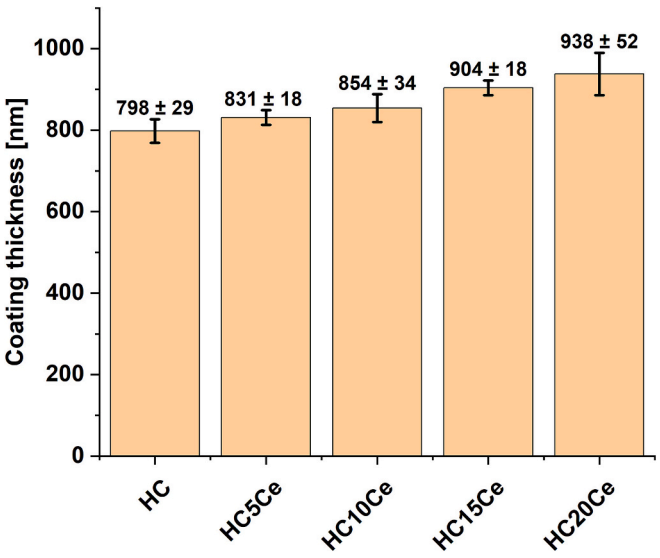

Fig. 2. Coating thickness without cerium HC, and with different cerium concentrations for 5 wt% (HC5Ce), for 10 wt% (HC10Ce), for 15 wt% (HC15Ce), for 20 wt% (HC20Ce).

The variations in coating thickness between the samples are relatively narrow and fall within the typical range of thin-film coatings commonly used for applications requiring precision and nanoscale uniformity. Therefore, the coatings remain categorised as thin films despite the increased thickness observed with higher cerium concentrations. This classification differentiates them from other protective coatings, such as paints or barrier coatings, which generally have thicknesses ranging from 10 μm to several hundred micrometres [66–68].

3.2. Light optical microscope analysis

In Fig. 3, light optical microscope images compare the appearance of HMDSO coatings when the coating is deposited with or without the simultaneous introduction of the cerium-containing aerosol. Fig. 3a shows a micrograph of coating HC exhibiting an almost uniform appearance. However, a few small, round dark spots are observed within the coating, which could be pinholes or other imperfections resulting from the plasma process conducted in an ambient atmosphere. Unlike the coating HC, coatings produced with cerium-containing aerosol appear more heterogeneous, suggesting that particle agglomerates, with sizes in the micro- and nanometre range, are distributed throughout the coating. For example, coating HC10Ce and HC20Ce are shown in Fig. 3b and c.

Additionally, increasing the cerium concentration in the aerosol increases the concentration of the particle agglomerations in the HMDSO coating, as visible in Fig. 3c for coating HC20Ce. Using the standard test method for determining volume fraction by systematic manual point count, (ASTM E562–02 [61]), microstructural analyses of light optical microscope images result in a particle volume fraction V_{CeO_2} of 1.42 ± 0.17 %, 2.28 ± 0.44 %, 3.45 ± 0.34 %, and 5.51 ± 0.82 % in HC5Ce, HC10Ce, HC15Ce, and HC20Ce, respectively. This investigation suggests that the agglomerates originate from the aerosol and cause variations in the coatings. It is proposed that particle agglomerations are most likely cerium-containing (cerium oxide, CeO_2) ones, which was confirmed by detailed TEM analyses (Section 3.5). It has to be considered that, the cerium is oxidised in the APPD process and incorporated into the HMDSO matrix, which consequently changes the concentration of cerium present in the coating compared to the concentration of the

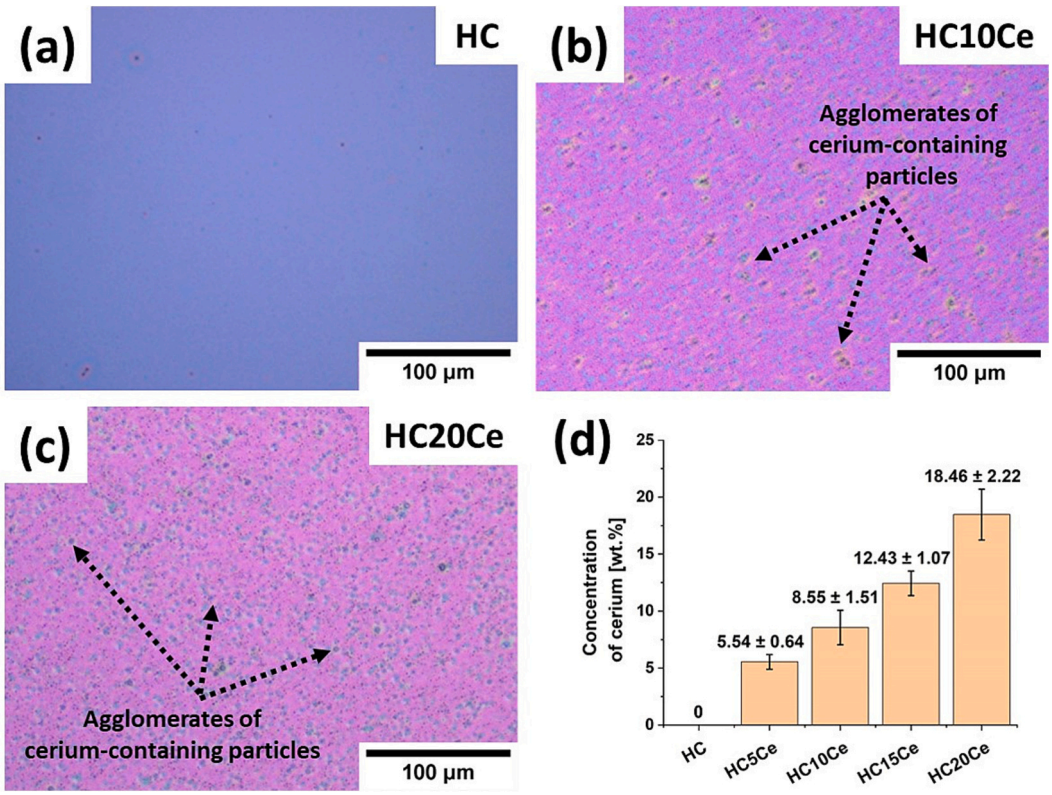

Fig. 3. Light optical microscope images of (a) HC, (b) HC10Ce, (c) HC20Ce, deposited on Si wafers, and (d) calculated concentration (wt%) of cerium in the coating.

prepared solution used for aerosolisation.

Thus, the concentration of cerium in the coating was calculated to further estimate the content present in the coatings (Fig. 6d). It is important to note that both results, consequently the volume fraction and the concentration, obtained from light optical microscope analyses tend to be overestimated. This overestimation occurs because both particles on the surface and embedded within the coating are included in the calculation, as they are visible through the transparent HMDSO coatings. However, the test method is intended for analysing a two-dimensional cross-section of the sample. Furthermore, images taken with the microscope may contain artefacts that are mistakenly interpreted as particles, although they are not actually ones and the manually counting is prone to subjective errors.

3.3. FTIR spectroscopy of coatings

Fourier transform infrared (FTIR) spectroscopy is a valuable analytical tool for verifying a coating formation and allows the derivation of a possible coating structure based on the position and shape of the absorption peaks. Therefore, spectroscopy of the uncoated AlSi10Mg0.3 substrate, the HMDSO precursor and the different coatings were analysed. Since the main observable differences of the absorption peaks are observed in the range of 1500–500 cm^{-1}, the zoomed spectra are displayed in the insert of Fig. 4 (see Table 2).

According to Möller et al. [69] the prominent absorption peaks of the HMDSO precursor can be found at: 754 and 846 cm^{-1} ($Si(CH_3)_x$ stretching mode), 1060 cm^{-1} (-Si-O-Si- stretching mode), 1260 cm^{-1} (Si$(CH_3)_3$ rocking), 1420–1450 cm^{-1} (-CH_3 bending mode), and 2850 and 2950 cm^{-1}(-CH_3 stretching). Most modes were also detected in the coatings spectra; however, the peaks changed, indicating different chemical structures of the formed HMDSO coating. The spectra show a broad and strong peak between 1000 and 1200 cm^{-1}, with a maximum close to 1055 cm^{-1}, originating from the -Si-O-Si- stretching mode. The appearance of this absorption peak is mainly influenced by the present Si—O bond angle, the chain length, and the number of oxygen substituents on the silicon atoms [33]. Grill et al. [70] describe that peak maxima at 1135 cm^{-1}, 1063 cm^{-1} and 1023 cm^{-1} refer to a “cage”, “network”, and “silicon suboxide” coating structure, respectively. Therefore, the analyses indicate formation of a siloxane “network” during the plasma processing, which also includes “cage”-like structured regions within its structure [71,72]. As the degree of cross-linking within the Si-O-Si structure network correlates with the resulting coating density [73], it is assumed from the analyses that a highly cross-linked and dense HMDSO coating was formed. Nevertheless, as with “cage”-like regions in the network, a reduced density is also expected.

The peak observed at 900 cm^{-1}, corresponding to Si-OH symmetric bending, suggests the presence of silanol groups [71], indicating regions of a lower degree of cross-linking as well. Besides, alteration of the absorption peaks, originating from various vibrational modes of the Si $(CH_3)_x$ structure, reflects a transition from a methyl-dominated silicon environment in the precursor to a siloxane network-dominated environment in the coating [74].

Furthermore, from the spectra, it is observed that the addition of cerium-containing aerosol generates modifications of the peaks, especially in the Si-O-Si peak. For HC20Ce and HC5C, there is a slight shift of the Si-O-Si absorption peaks to higher wavenumbers and a broadening of the peak, implying an increased amount of “cage”-like regions in the coating. This effect can also be observed for HC15Ce, although not that strongly. For HC10Ce, a minimal peak shift to lower wave numbers is detected, indicating a more dense “network” structure with fewer “cage”-like regions. Additionally, a relatively low absorbance of the symmetric bending of Si-OH groups is observed in its spectrum, suggesting a more densely packed siloxane network.

Although the spectra reveal the chemical structure of the coatings, they do not provide detailed insights into cerium-containing particle agglomerations incorporated in the coating. This limitation arises due to overlapping absorption peaks of Si—O bending vibrations between 400 and 550 cm^{-1} [75] and the characteristic stretching vibration of cerium

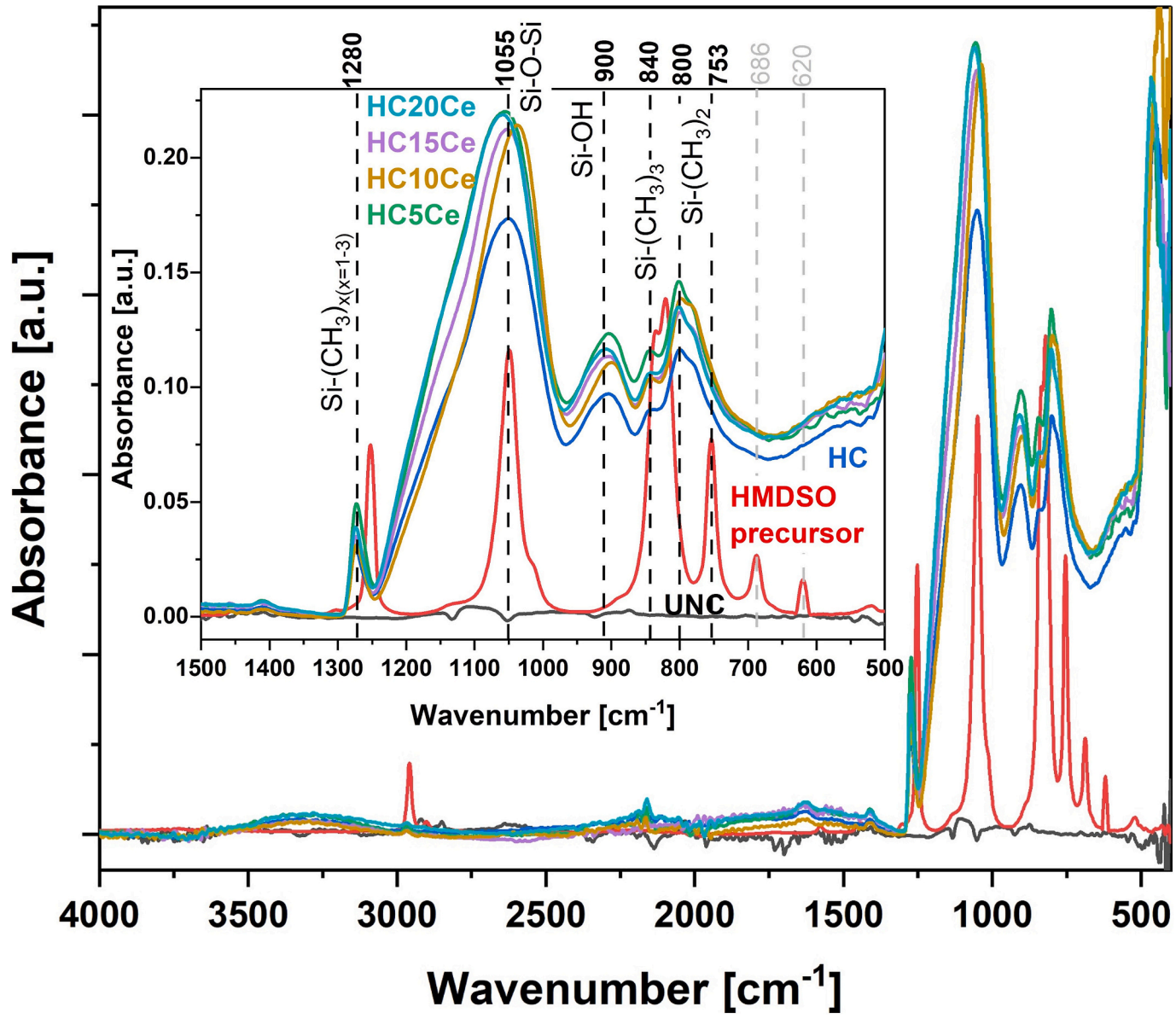

Fig. 4. FTIR spectra of the HMDSO precursor, uncoated AlSi10Mg0.3 (UNC), and AlSi10Mg0.3 coated with HC, HC5Ce, HC10Ce, HC15Ce and HC20Ce. Insert image presents the characteristic bands zoomed from the spectra.

oxide (Ce—O) at 450 cm^{-1} [76].

3.4. Corrosion testing using potentiodynamic polarisation measurements

Potentiodynamic polarisation (PDP) measurements were performed to evaluate the corrosion protection properties of the coating. PDP curves of uncoated AlSi10Mg0.3 (UNC) and coated samples with HC, HC5Ce, HC10Ce, HC15Ce and HC20Ce are shown in Fig. 5, while the determined electrochemical corrosion parameters from the Tafel extrapolations are given in Fig. 6 (Table S1).

The barrier protection of the coatings can be observed as the corrosion current density (j_{corr}) of the uncoated sample ($6{,}0 \times 10^{-7}$ Acm^{-2}) is reduced by the application of the coatings. In addition to coating thickness and composition, the cerium concentration affects the coating performance. Adding a cerium-containing aerosol during APPD, significantly reduces the corrosion current density of the sample, enhancing the corrosion resistance of AlSi10Mg0.3. While the sample coated with HC shows a corrosion current density of 4.8×10^{-8} Acm^{-2}, the coatings produced with the addition of cerium-containing aerosols show one of 5.6×10^{-9}, 3.8×10^{-9}, 2.7×10^{-9}, 2.9×10^{-9} Acm^{-2} for HC5Ce, HC10Ce, HC15Ce and HC20Ce, respectively (Fig. 6a, Table S1).

Further electrochemical corrosion parameters (E_{bd}, E_{corr}, and $\Delta E = |E_{bd} - E_{corr}|$) plotted against cerium concentration are summarised in Fig. 6b-d, Table S1. While the uncoated sample (UNC) shows the lowest breakdown potential ($E_{bd} = -0.57$ *V*) based on the poor breakdown corrosion resistance of AlSi10Mg0.3, coating HC shows the highest ($E_{bd} = -0.20$ V), Fig. 6b. Coatings produced with intermediate cerium concentrations in the aerosol (HC10Ce, HC15Ce) show a gradual increase in $E_{bd,}$ reflecting an enhancement in their corrosion resistance. But HC20Ce (with great amount of cerium oxide particles) exhibits a more negative E_{bd} (−0.83) V, suggesting the lowest resistance to local coating breakdown among all coatings.

A decrease in E_{corr} is observed for all coated samples (Fig. 6c, Table S1).This shift towards more negative potentials is attributed to the barrier effect of the coating and increased oxidation reactions facilitated by cerium. Although cerium is mainly present as CeO_2 in the coating, environmental conditions and chemical interactions such as localised acidic conditions, can facilitate a release of Ce^{3+} ions [77,78]. The ions

Table 2
Assignment of the FTIR absorption peaks.

Assignments	Peaks (cm^{-1})	References
Precursor		
-CH_3 Stretching	2850, 2950	[69]
-CH_3 Bending Mode	1420–1450	[69]
$Si(CH_3)_3$ Rocking	1260	[69]
-Si-O-Si-O-Si- Stretching Mode	1060	[69]
$Si(CH_3)_x$ Stretching Mode	754, 846	[69]
HMDSO coatings		
$Si(CH_3)_3$ Rocking	1280	[69]
"Network" Structure (-Si-O-Si- Stretching)	1055	[70]
Si-OH Symmetric Bending (Silanol-groups)	900	[71]
$Si(CH_3)_x$ Stretching Mode	840, 800	[74]
Si-O Bending	400–550	[75]
Ce–O Stretching	450	[76]
Classification of siloxane coatings by Grill et al.		
"Cage" Structure (-Si-O-Si- Stretching)	1135	[70]
"Network" Structure (-Si-O-Si- Stretching)	1063	[70]
"Silicon Suboxide" Structure (-Si-O-Si- Stretching)	1023	[70]

are soluble and can migrate through the coating, re-oxidise at different locations, and contribute to a passivation by forming Ce-hydroxide, which subsequently oxidises further to Ce-oxide [46–50]. With higher cerium concentrations, oxidation reactions occur more frequently during electrochemical testing, shifting E_{corr} into a more negative (non-noble) region [45,46,48]. These oxidation reactions (Ce-hydroxide → Ce-oxide) seal defect sites in the coating and extend the passive region in the anodic branches (for HC5–HC15).

However, the enhancement in corrosion resistance provided by the coatings is evident in Fig. 6d, which shows ΔE for the individual samples. A larger ΔE indicates improved barrier protection, which is critical for long-term corrosion resistance. The data reveal that both the HMDSO coating (HC) and coatings produced with the addition of cerium-containing aerosol during APPD (HCxCe) positively influence ΔE, thereby significantly enhancing the corrosion resistance of AlSi10Mg0.3.

The best barrier protection was observed in HC ($\Delta E = 0.51\ V$), while the optimal cerium concentration of the aerosol lies in the range of 10 to 15 wt% ($\Delta E = 0.46$, and 0.47 V). A further increase in cerium concentration (HC20Ce) reduces the barrier protection, likely due to structural changes within the coating resulting from excessive cerium content. This aligns with previous findings that excessive cerium loading can negatively affect coating integrity by introducing porosity or internal stress, as reported in the literature [51,53].

3.5. Coating analysis using TEM

Detailed microstructure analyses using the TEM technique in BF mode were performed on thin foils of selected HMDSO coatings, HC and HC10Ce (Fig. 7) to investigate the role of particle agglomerates observed in a light optical microscope, which were held to be responsible for the different corrosion properties of the coatings. Observation of the coatings in cross-section allowed us to estimate their thickness (~800 nm), which correlates well to thickness measurements carried out on Si wafer pieces. Furthermore, good adhesion of the coating on the ground AlSi10Mg0.3 substrate can be detected, which results from the plasma pretreatment. In Fig. 7a, coating HC is shown. It appears homogeneous over the entire coating thickness. Comparing HC with HC10Ce (Fig. 7b), particles in the size of a few tens of nanometres were incorporated in the coating. These nanoparticles are well connected to the HMDSO matrix, showing no pores around the particles.

Furthermore, a relatively uniform particle distribution was observed, consistent with the appearance of the coating already seen under the light optical microscope. An EDXS analysis was carried out to qualitatively analyse the chemical composition of both, the coating and the nanoparticles (Fig. 8a). This result reveals the presence of cerium-containing nanoparticles. Line spectra analysis shows that nanoparticles are instead containing oxide and are not pure cerium (Fig. 8b and c). This confirms that cerium-containing aerosols varies the coatings composition, as already suggested from light optical microscope analyses.

Additionally, the HMDSO matrix and the nanoparticles were investigated in terms of their microstructure. The selected area electron diffraction pattern shows an amorphous matrix formed by the Si-O-Si

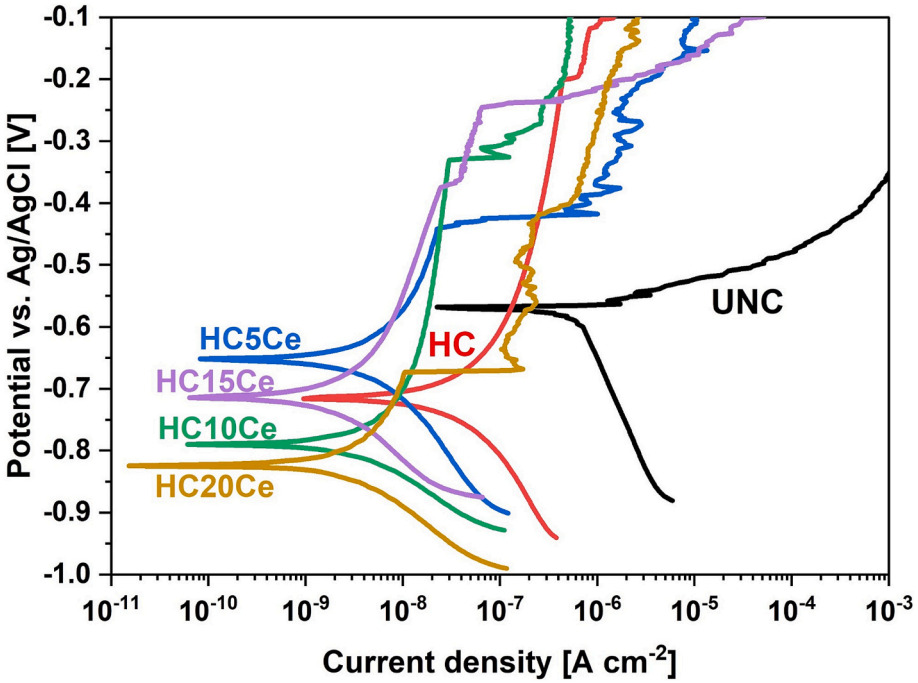

Fig. 5. Potentiodynamic polarisation (PDP) curves of uncoated AlSi10Mg0.3 (UNC) and AlSi10Mg0.3 coated with HC, HC5Ce, HC10Ce, HC15Ce and HC20Ce.

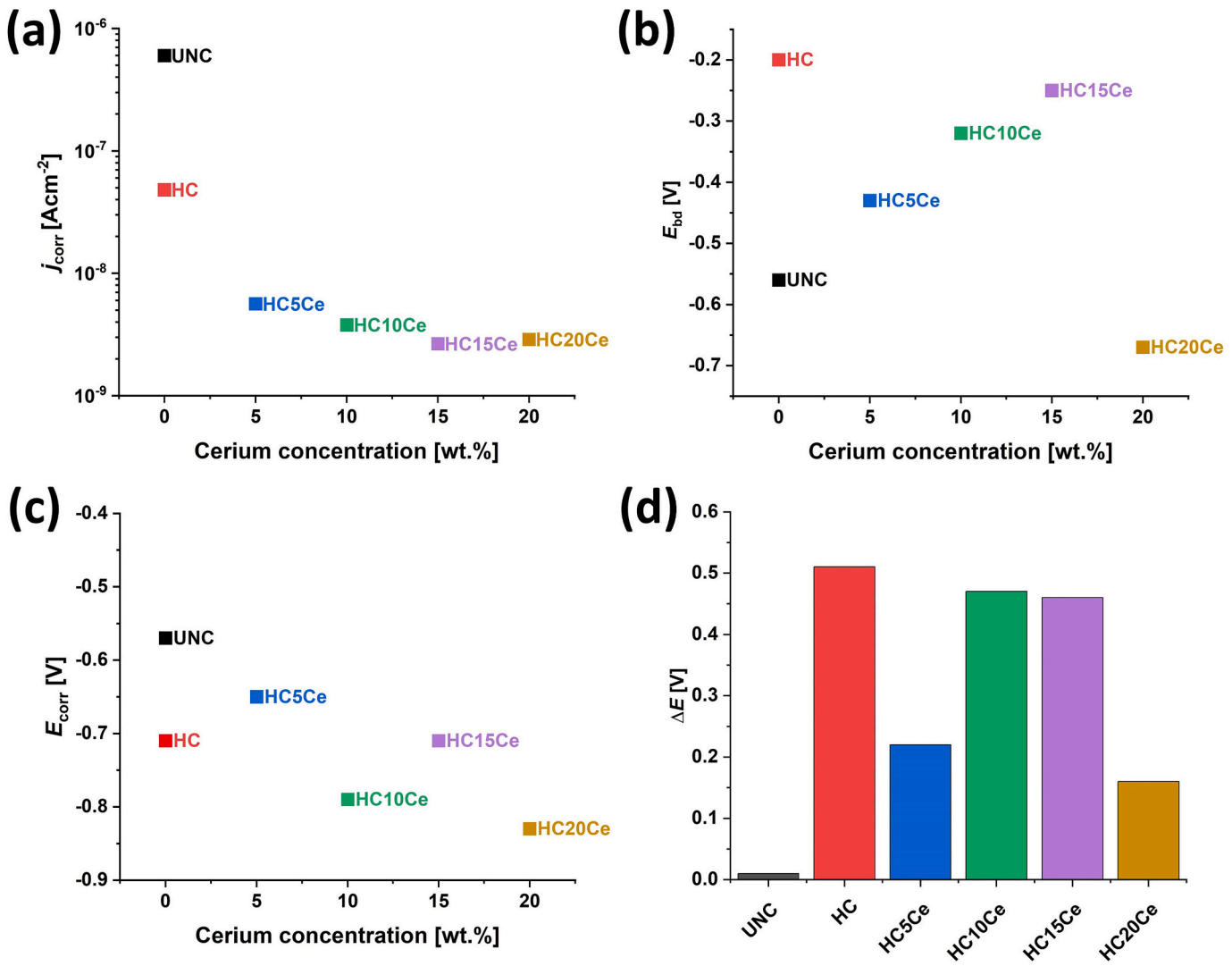

Fig. 6. (a) Corrosion current density j_{corr} (b) coating breakdown potential E_{bd} (c) corrosion potential E_{corr} and (d) $\Delta E = |E_{bd} - E_{corr}|$ plotted against cerium concentration evaluated by potentiodynamic polarisation measurements presented in Fig. 5.

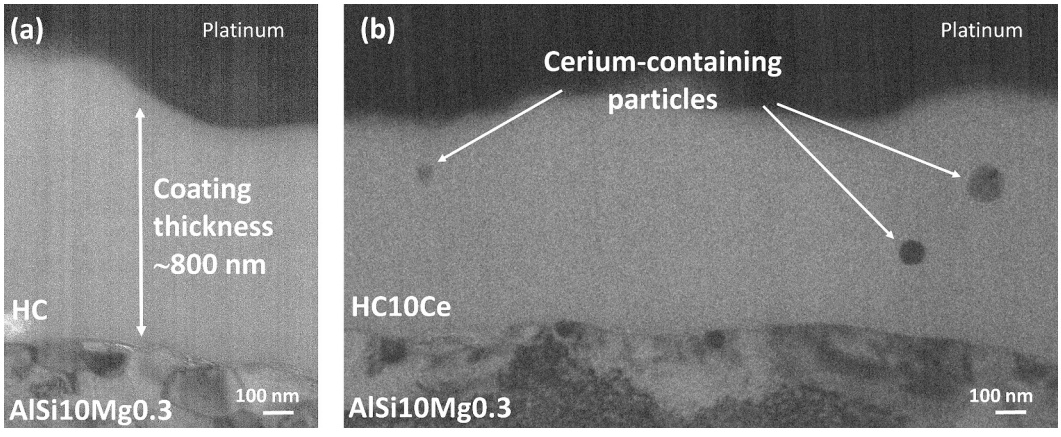

Fig. 7. TEM BF image of (a) HC and (b) HC10Ce deposited on AlSi10Mg0.3.

network, as indicated by FTIR measurements, and polycrystalline nanoparticles. HRTEM analyses and Inverse Fast Fourier transformation (IFFT) confirmed the presence of a hexagonal cerium dioxide (CeO_2) phase within the particles present (Fig. 9). The crystal formation can be explained by the oxidation of cerium ions, according to reactions (1–3) [79], which take place during the APPD process.

$$Ce^{3+} - e^- \rightarrow Ce^{4+} \quad (1)$$

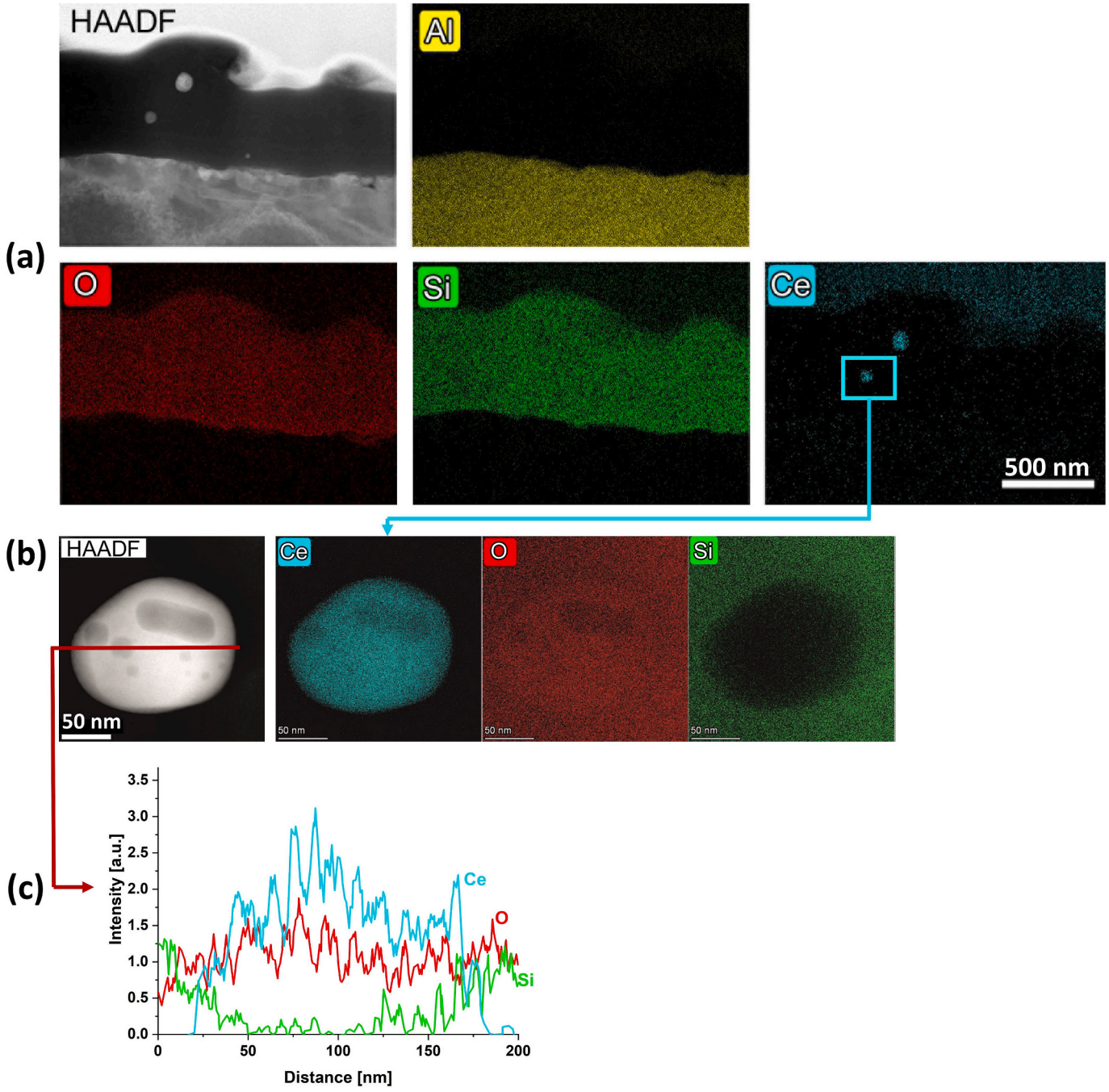

Fig. 8. (a) EDS mapping of HC20Ce deposited on AlSi10Mg0.3, (b) EDS mapping of the cerium-containing particle incorporated in the coating and (c) EDS line profile performed at the particle.

$$Ce^{4+} + 4OH^{-} \rightarrow Ce(OH)_4 \quad (2)$$

$$Ce(OH)_4 \rightarrow CeO_2 + 2\,H_2O \quad (3)$$

These investigations validate the structural differences in the coatings. Polycrystalline nanoparticles are more densely packed than the amorphous HMDSO matrix, contributing to an overall increase in coating density. Additionally, as already observed in light optical microscope analyses, increasing the cerium concentration leads to a higher occurrence of particle agglomerates in the coating, further enhancing its overall density.

The images of the sample HC10Ce were used to further quantify the atomic concentration of cerium in the coating. For this, the same test method as applied on the light optical microscope images was carried out. However, the grid of points were configured to the scale of the images (308 points). The evaluated average volume fraction V_{CeO_2} of particles results in 1.31 ± 0.54 % and a concentration of cerium was calculated to be 5.47 ± 0.67 wt%, which is slightly lower than the estimated concentration from the light optical microscope image (8.55 ± 1.51 wt% for HC10Ce).

3.6. Corrosion testing in salt-spray chamber

Mechanically ground AlSi10Mg0.3 samples coated with HMDSO and cerium-containing aerosol (HC and HCxCe) were exposed to salt-spray to investigate the coatings' long-term corrosion performance. The

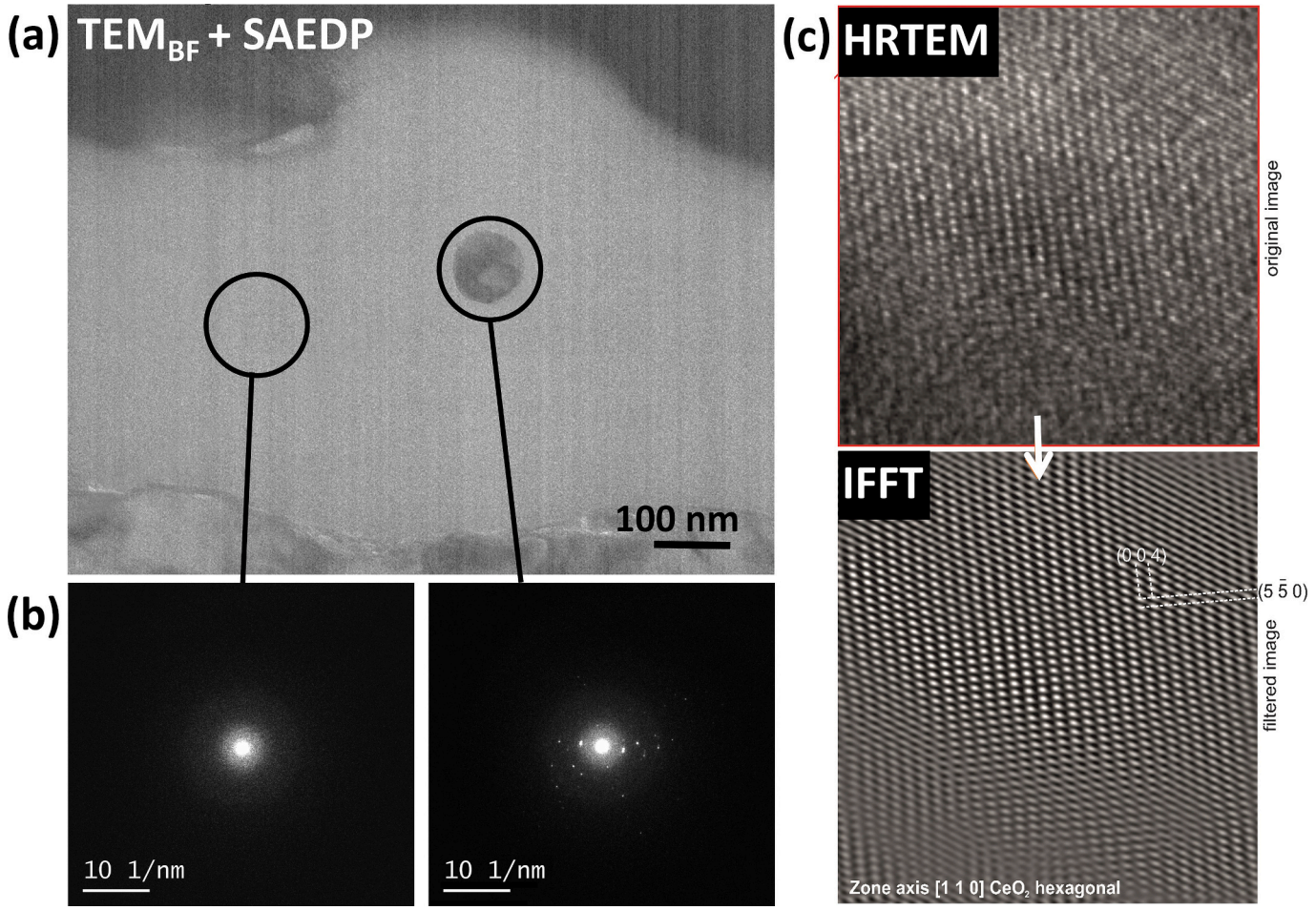

Fig. 9. TEM analysis of a cross-section of HC10Ce deposited on AlSi10Mg0.3 performed by (a) SAEDP, (b) diffraction pattern of the coating and the cerium-containing particle and (c) HRTEM and Inverse Fast Fourier transformation (IFFT) image of the particle.

samples were compared to an uncoated reference sample (UNC). Fig. 11a depicts the samples directly before the salt-spray chamber test. Figure S3 (Supplementary Material) illustrates their condition after 3 weeks of testing, and Fig. 10b shows the samples after 6 weeks. The protective effect of the coatings is evident already after 3 weeks. While the uncoated sample exhibited a fully corroded surface, all the coated samples retained their metallic sheen. This trend continued to the end of the test at 6 weeks, where coated samples showed only localised spots of corrosion. Thus, it confirms the effective corrosion resistance provided by the various types of the relatively thin HMDSO coatings. As indicated by the results of the PDP measurements, the salt-spray chamber test further confirms the enhanced protective effect of cerium. Samples coated with cerium-containing HMDSO coatings performed better, exhibiting even less localised corrosion compared to the sample coated with undoped HMDSO (Fig. 10b and c). The results of the quantitative photo analysis, shown in Fig. 11, indicate that a cerium concentration of 5 wt% or, preferably, 10 wt% in the aerosol is required to fully utilise the corrosion protection effect of cerium-containing HMDSO coatings.

To investigate the corrosion protection of cerium-containing HMDSO coatings in more detail, SE micrographs and EDXS of the uncoated and coated AlSi10Mg0.3 were taken before and after the salt-spray chamber test. Fig. 12a-c representatively show SE micrographs of UNC, HC, and HC10Ce before testing, associated surface element distribution measured by EDXS are depicted in the circle charts below (Fig. 12d-f). Further micrographs and results of the EDXS can be found in the supplementary material (Figures S6 and S7, Tables S1and S2). The HMDSO layer cannot be identified from the SE micrographs alone. However, when comparing the element distributions of the uncoated to the coated samples, the presence of the deposited HMDSO coating becomes evident due to the increased silicon and oxygen concentrations and the simultaneous decrease in aluminium content. Despite cerium is present in detectable amounts using light optical microscope and TEM analyses, cerium was not measured in EDXS, likely due to the signal dominance of aluminium, oxygen, carbon and silicon, as predominant elements as well as the low magnification, which further reduces the sensitivity to its detection. The microscopic investigations of the samples after the salt-spray chamber test confirmed the values obtained from PDP measurements as well as the qualitative and quantitative results of the salt-spray chamber test (Fig. 13). The corrosion attack of the entire uncoated AlSi10Mg0.3 surface is visible, as the ground surface is not flat anymore and is covered with corrosion products. In Fig. 13b and c, the protective characteristics of the HMDSO coatings are visible, as the surface of the samples is significantly less corroded compared to the uncoated sample. The coatings effectively reduce the exposure of the underlying metal to the corrosive media preserving the ground appearance, demonstrating effective protection against corrosion, which can also be determined from the EDXS. Whereas, the uncoated sample experienced a significant depletion of aluminium and the oxygen concentration highly increased, the element distributions of the coated samples insignificantly changed. The effect of incorporated cerium is apparent when comparing the micrographs from coating HC to HC10Ce. While localised corrosion and formation of corrosion products can be detected on sample coated with HC, the sample coated with HC10Ce demonstrates an almost fully protected surface, with the cerium incorporation further enhancing the coating's protective performance. The minor shift in the oxygen concentration in the EDXS of HC can likely be attributed to the corrosion of

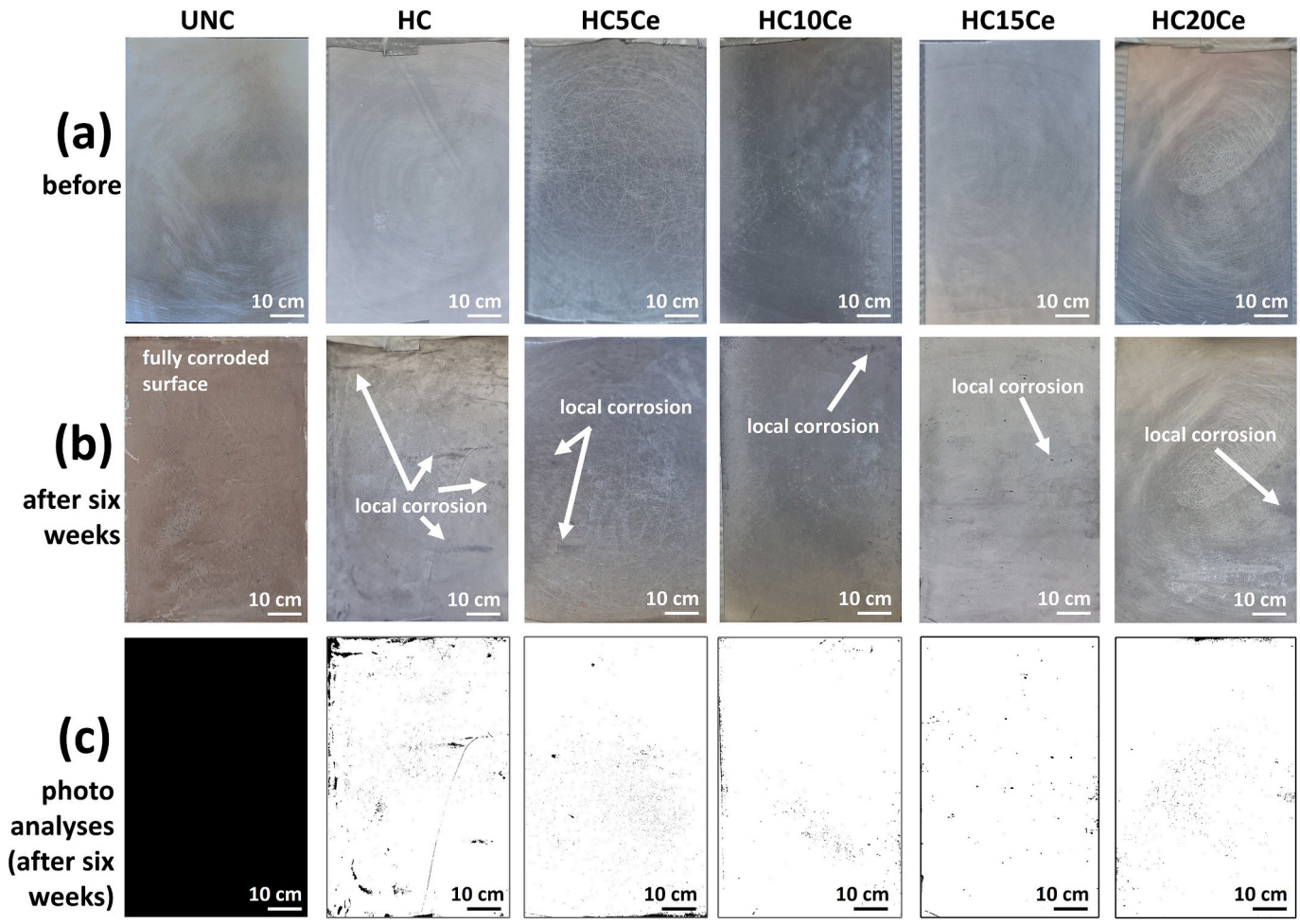

Fig. 10. The surface appearance of mechanically ground AlSi10Mg0.3, including the uncoated sample and coated samples, (a) before the salt-spray test and (b) after 6 weeks of testing. (c) Results of the photo analysis of Fig. 10b using ImageJ.

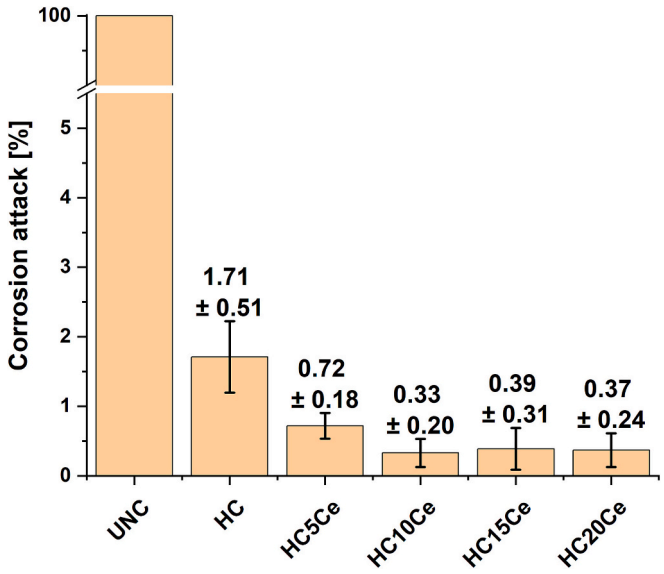

Fig. 11. Quantitative results of the corrosion attack after 6 weeks of salt-spray testing obtained from photos depicted in Fig. 10c using ImageJ.

the AlSi10Mg0.3 substrate with Al_2O_3 and $Al(OH)_3$ as the typical corrosion products of the alloy.

3.7. Protection mechanism and its limitations

Based on the described results, a schematic corrosion protection model was developed for L-PBF-fabricated AlSi10Mg0.3, as shown in Fig. 14.

Coating characterisations showed that the APPD of HMDSO, along with the aerosol, enables the production of coatings a few hundred nanometres thick. While the coating formed from HMDSO alone appears dense and uniform, consisting of an amorphous siloxane network, the addition of a cerium-containing aerosol results in a heterogeneous coating, where the siloxane network serves as a matrix for CeO_2 nanoparticles formed during the plasma process. Besides this, a good adhesion of the HMDSO coatings to the metal surface was achieved. Results of PDP measurements demonstrate that the undoped HMDSO coating (HC) notably protects the metal surface from corrosion. However, salt-spray chamber tests have also revealed that the long-term protection performance of the coating is limited. One reason for that can be the "cage"-like structured regions with a less densely packed siloxane network within the coating, enabling electrolyte (corrosion medium, $NaCl_{(aq)}$) to gradually penetrate the coating and potentially reducing the corrosion resistance over time.

Additionally, it is assumed from light optical microscope analysis that imperfections, such as small pinholes, are present in the coating. These defects decrease the coating's corrosion resistance by also

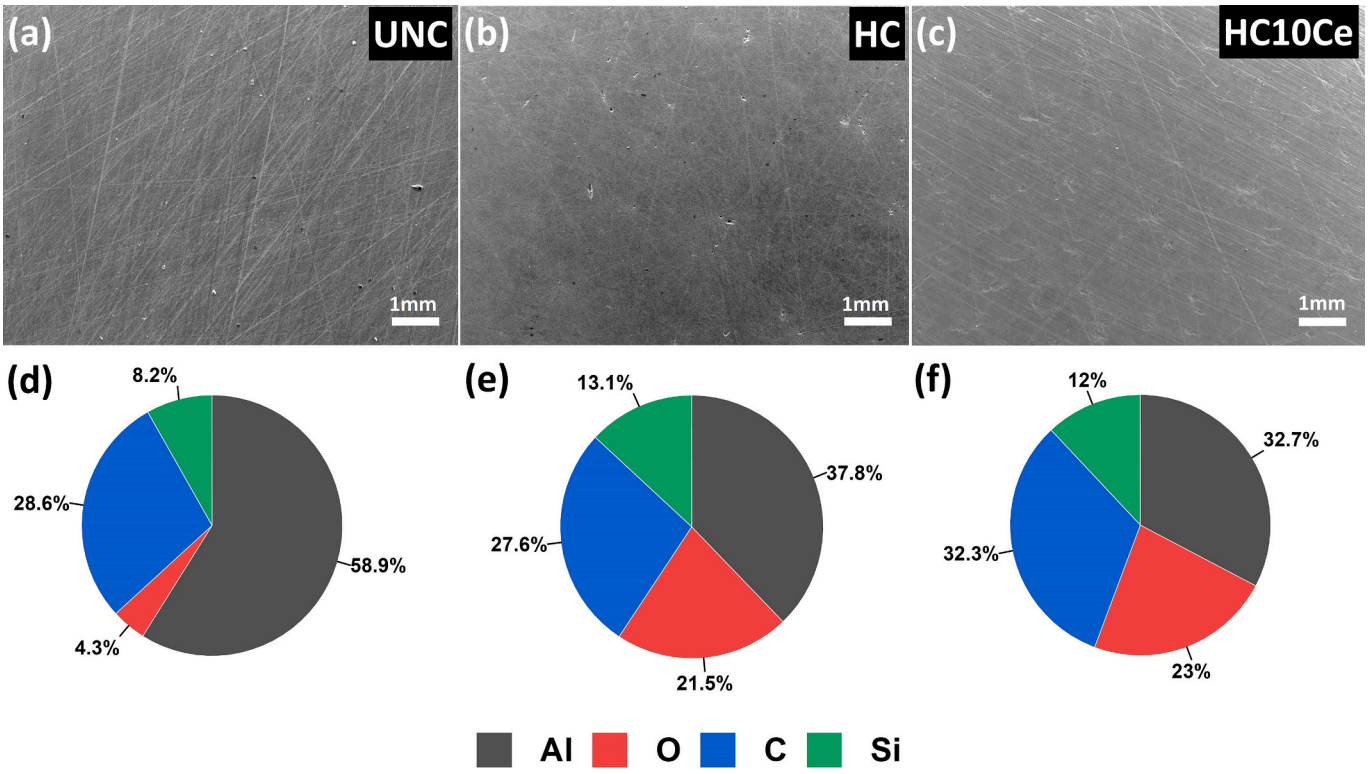

Fig. 12. SE micrographs taken before salt-spray chamber test of (a) uncoated sample (UNC), (b) sample coated with HC, and (c) sample coated with HC10Ce. The associated surface element distribution measured by EDXS are depicted below the respective micrograph in the circle charts in (d-f).

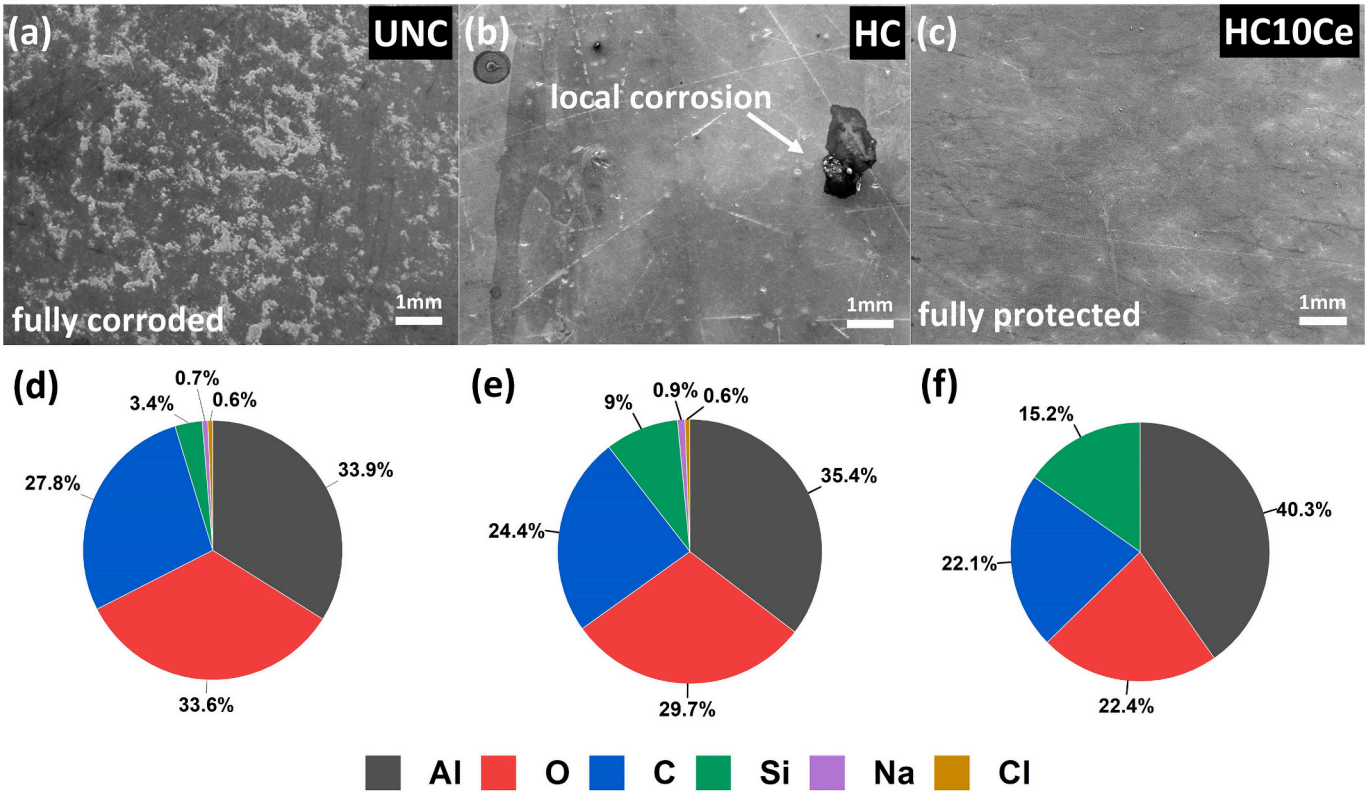

Fig. 13. SE micrographs taken after salt-spray chamber test of (a) uncoated sample (UNC), (b) sample coated with HC, and (c) sample coated with HC10Ce. The associated surface element distribution measured by EDXS are depicted below the respective micrograph in the circle charts in (d-f).

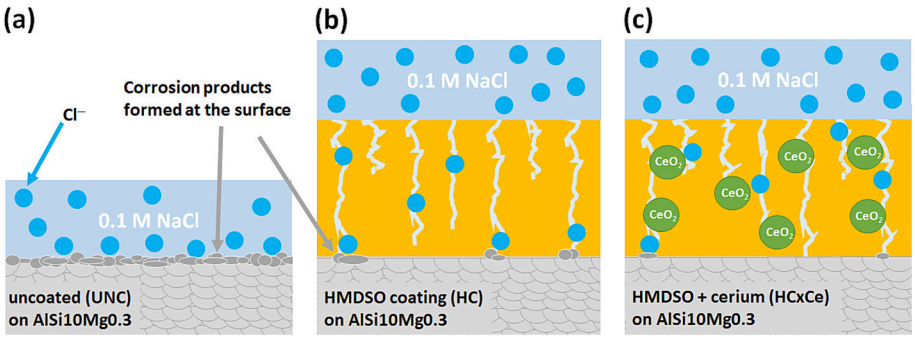

Fig. 14. Explanation of the protection mechanism of the studied coatings. (a) An uncoated L-PBF-fabricated AlSi10Mg0.3 fully corrodes in the presence of NaCl solution. (b) Undoped HMDSO coating (HC) deposited on AlSi10Mg0.3 offer corrosion protection; however, localised corrosion occurs due to imperfections and less densely packed regions within the coating. (c) HMDSO coating produced with cerium-containing aerosol (HCxCe) contains CeO_2 nanoparticles, which improve the corrosion protection by preventing the electrolyte from penetrating the coating, thereby providing even better protection to the AlSi10Mg surface.

facilitating the electrolyte's penetration. As a result, Cl^- ions are present at the interface, promoting localised corrosion and degradation of the AlSi10Mg0.3 substrate (Fig. 14b).

Thus, an important improvement in the corrosion resistance of the coating found in this study is the incorporation of CeO_2 nanoparticles into the HMDSO coating by utilising a cerium-containing aerosol during APPD. Light optical microscope and TEM analysis showed the presence of these particles, which were identified as CeO_2 nanoparticles. These polycrystalline nanoparticles are effectively integrated into the HMDSO coating. As observed from corrosion tests, this results in enhanced corrosion resistance of the HMDSO coatings. The improved protection can be explained by increased coating density due to CeO_2 particles. They act as barriers and hinder the diffusion of Cl^- ions to the substrate (Fig. 14c). This result shows the beneficial influence of adding cerium-containing aerosol in the APPD process. However, due to the aerosol addition and modifications of the APPD process with overlapping effects of interacting reactions [80], a possible promotion to the formation of regions with a "cage "-like structure was found in FTIR spectra of coatings produced with low and high cerium concentrations (HC5Ce and HC20Ce, respectively). These findings mainly affected the corrosion resistance of HC5Ce, as revealed in corrosion tests. Coatings produced with cerium concentration higher than 10 wt% in the aerosol exploit the incorporation of CeO_2 nanoparticles as dense filling and showed improved corrosion resistance compared to the other coatings studied here. At this point, it should be noted that further enhancement of the protection performance is challenging to achieve in the used process configuration. On the one hand, it was observed in FTIR spectroscopy that higher cerium concentrations lead to a less cross-linked and more porous siloxane network. However, 20 wt% of cerium is close to the saturation limit of the solution used for the aerosol generation. Therefore, a high viscosity of the solution was observed, which hindered consistent aerosol generation during the deposition process.

Since only a small amount of CeO_2 particle agglomerates was detected in the coatings (an area fraction of max. 5 % in HC20Ce), it is hypothesized that a part of the introduced cerium remained as Ce^{3+} and Ce^{4+} ions introduced in the coatings and can act there as active corrosion inhibitors. However, the main aim of this study was to analyse the barrier protection of the coatings. The tests did not focus on whether cerium ions were present in the coatings, and active protection was not studied in detail. These effects can be analysed in the next step to improve the corrosion protection of cerium-containing HMDSO coatings further.

4. Conclusions

This study investigated the formation of cerium-containing HMDSO coating with an aerosol-assisted atmosphere pressure plasma deposition (APPD) and its corrosion protection performance on L-PBF-fabricated AlSi10Mg0.3 substrates. The key findings can be summarised as follows:

- Undoped and cerium-doped HMDSO coatings were efficiently deposited on AlSi10Mg0.3 substrates, with an approximate thickness of 800 nm.
- Samples with low and high cerium concentrations exhibit "cage-like" structured regions in the coating, characterised by FTIR spectroscopy. These regions can be related to a less cross-linked siloxane network and consequently a minimally reduced protection.
- TEM analysis confirmed that the presence of CeO_2 nanoparticles contributed to changes in the coating structure.
- Potentiodynamic polarisation measurements confirmed that the undoped HMDSO coating reduced corrosion current density compared to the uncoated AlSi10Mg0.3 alloy, indicating barrier corrosion protection. The addition of cerium, with an optimal concentration of 10 wt% in the aerosol solution, showed lower corrosion current density than the coating without cerium, indicating optimal barrier protection.
- Incorporated CeO_2 nanoparticles mitigate the limitations caused by structural defects of the HMDSO coating and prevent penetration of the chloride ions from the corrosive environment.
- Moreover, the salt-spray test, according to ASTM B117–23, confirmed the durability of corrosion protection for up to 6 weeks. The most protected was alloy coated with HC10Ce.

This study showed that cerium-containing HMDSO coating serves as a good alternative for corrosion protection, providing passive barrier protection for L-PBF-fabricated AlSi10Mg0.3 alloy. Future work should focus on the detailed investigation of cerium within the coating and the possibility of active corrosion protection with cerium to optimise the protective performance of cerium-containing HMDSO coatings processed by aerosol-assisted APPD.

CRediT authorship contribution statement

Mirjam Spuller: Writing – original draft, Visualization, Validation, Project administration, Methodology, Investigation, Formal analysis, Data curation, Conceptualization. **Nina Kovač:** Writing – review & editing, Visualization, Validation, Methodology, Investigation, Formal analysis, Data curation, Conceptualization. **Peter Rodič:** Writing – review & editing, Visualization, Validation, Supervision, Project administration, Methodology, Investigation, Funding acquisition, Formal analysis, Data curation, Conceptualization. **Lukasz Major:** Writing – review & editing, Visualization, Validation, Methodology, Investigation, Formal analysis, Data curation, Conceptualization. **Simon Chwatal:** Writing – review & editing, Visualization, Supervision, Investigation, Formal analysis. **Mattia Cabrioli:** Resources. **Matteo Vanazzi:** Resources. **Giorgio De Pasquale:** Project administration, Funding

acquisition. **Juergen M. Lackner:** Supervision, Project administration, Methodology, Funding acquisition, Conceptualization. **Reinhard Kaindl:** Writing – review & editing, Supervision. **Wolfgang Waldhauser:** Writing – review & editing, Supervision.

Declaration of Generative AI and AI-assisted technologies in the writing process

During the preparation of this work, the author(s) used ChatGPT, OpenAI to assist in sentence editing. After using this tool/service, the author(s) reviewed and edited the content as needed and take(s) full responsibility for the publication's content.

Funding

This work has been financed by Horizon Europe MIMOSA Project, G. A. Number: 101091826 under the Call HORIZON-CL4–2022-RESILIENCE-01, from the Slovenian Research and Innovation Agency: research core funding No. P1–0134 and OeAD – Agency for Education and Internalisation, project WTZ – SI18/2023.

Declaration of competing interest

The authors declare that they have no known competing financial interests or personal relationships that could have appeared to influence the work reported in this paper.

Acknowledgements

Thanks go to Harald Parizek for conducting coating deposition and characterisation experiments and to Roswitha Elter, who performed SEM analysis. The authors also acknowledge the Slovenian Research and Innovation Agency (ARIS) for funding the bilateral project between Slovenia and Austria titled Atmospheric pressure plasma deposited coatings synthesis and characterisation (grant No. BI-AT/24-24-017) and OeAD – Agency for Education and Internalisation, project WTZ – SI18/2023.

Appendix A. Supplementary data

Supplementary data to this article can be found online at https://doi.org/10.1016/j.surfcoat.2025.132094.

Data availability

Data will be made available on request.

References

[1] J. Preußner, G. Rödler, F.G. Fischer, K. Hintz, V. Friedmann, A. Weisheit, Additive manufacturing of a lightweight Al-ca alloy by direct energy deposition and laser powder bed fusion, practical, Metallography 60 (2023) 704–715, https://doi.org/10.1515/pm-2023-0062.
[2] V.S. Zolotorevsky, N.A. Belov, M.V. Glazoff (Eds.), Casting Aluminum Alloys, Elsevier, Amsterdam, 2007.
[3] H. Fan, F. Ann Witvrouw, R. Wolf-Monheim, S. Yang Souschek, Effects of substrate surface treatments on hybrid manufacturing of AlSi7Mg using die casting and selective laser melting, journal of material, Sci. Technol. 156 (2023) 142–156, https://doi.org/10.1016/j.jmst.2023.02.009.
[4] P.A. Rometsch, Y. Zhu, X. Wu, A. Huang, Review of high-strength aluminium alloys for additive manufacturing by laser powder bed fusion, Mater. Des. 219 (2022) 110779, https://doi.org/10.1016/j.matdes.2022.110779.
[5] H. Chen, C. Zhang, D. Jia, D. Wellmann, W. Liu, Corrosion behaviors of selective laser melted aluminum alloys: a review, Metals 10 (2020) 102, https://doi.org/10.3390/met10010102.
[6] A. Gatto, C. Cappelletti, S. Defanti, F. Fabbri, The corrosion behaviour of additively manufactured AlSi10Mg parts compared to traditional Al alloys, Metals 13 (2023) 913, https://doi.org/10.3390/met13050913.
[7] Y. Zheng, Z. Zhao, R. Xiong, G. Ren, M. Yao, W. Liu, L. Zang, Effect of post heat treatment on microstructure, mechanical property and corrosion behavior of AlSi10Mg alloy fabricated by selective laser melting, Prog. Nat. Sci. Mater. Int. 34 (2024) 89–101, https://doi.org/10.1016/j.pnsc.2024.02.001.
[8] N. Read, W. Wang, K. Essa, M.M. Attallah, Selective laser melting of AlSi10Mg alloy: process optimisation and mechanical properties development, Mater. Des. 65 (2015) (1980-2015) 417–424, https://doi.org/10.1016/j.matdes.2014.09.044.
[9] J.M. Lackner, R. Kaindl, A. Schwan, B. Meier, S. Augl, S. Gumus, A. Hinterer, M. Stummer, Atmosphärische Plasmabeschichtung: mit aktiven Korrosionsschutz-Beschichtungen für 3D-Druck Aluminium-Bauteile, Jahrbuch - Oberflächentechnik (2021) 1–24.
[10] F. Trevisan, F. Calignano, M. Lorusso, J. Pakkanen, A. Aversa, E.P. Ambrosio, M. Lombardi, P. Fino, D. Manfredi, On the selective laser melting (SLM) of the AlSi10Mg alloy: process, microstructure, and mechanical properties, Materials 10 (2017) 76, https://doi.org/10.3390/ma10010076.
[11] K. Kempen, L. Thijs, J. van Humbeeck, J.-P. Kruth, Mechanical properties of AlSi10Mg produced by selective laser melting, Phys. Procedia 39 (2012) 439–446, https://doi.org/10.1016/j.phpro.2012.10.059.
[12] O. Maurer, F. Herter, D. Bähre, The impact of manufacturing parameters on corrosion resistance of additively manufactured AlSi10Mg-samples: a design of experiments approach, Manufact. Lett. 34 (2022) 29–33, https://doi.org/10.1016/j.mfglet.2022.08.006.
[13] P. Fathi, M. Rafieazad, X. Duan, M. Mohammadi, A.M. Nasiri, On microstructure and corrosion behaviour of AlSi10Mg alloy with low surface roughness fabricated by direct metal laser sintering, Corros. Sci. 157 (2019) 126–145, https://doi.org/10.1016/j.corsci.2019.05.032.
[14] M. Cabrini, F. Calignano, P. Fino, S. Lorenzi, M. Lorusso, D. Manfredi, C. Testa, T. Pastore, Corrosion behavior of heat-treated AlSi10Mg manufactured by laser powder bed fusion, Materials (Basel) 11 (2018), https://doi.org/10.3390/ma11071051.
[15] Z. Zhang, B. Wang, Z. Zhao, X. Li, B. Liu, P. Bai, Effect of chloride ion concentration on corrosion process of selective laser melted AlSi10Mg with different heat treatments studied by electrochemical noise, J. Mater. Res. Technol. 16 (2022) 1597–1609, https://doi.org/10.1016/j.jmrt.2021.12.102.
[16] P.L. Hagans, C.M. Haas, Chromate Conversion Coatings, ASM International, Ohio, 1994.
[17] ECHA - Eur. Chem. Agency, 2024. https://echa.europa.eu/ (accessed 28 November 2024).
[18] M. Becker, Chromate-free chemical conversion coatings for aluminum alloys, Corros. Rev. 37 (2019) 321–342, https://doi.org/10.1515/corrrev-2019-0032.
[19] O. Gharbi, S. Thomas, C. Smith, N. Birbilis, Chromate replacement: what does the future hold? npj Mater. Degrad. 2 (2018) 1–8, https://doi.org/10.1038/s41529-018-0034-5.
[20] R.M. Park, J.F. Bena, L.T. Stayner, R.J. Smith, H.J. Gibb, P.S.J. Lees, Hexavalent chromium and lung cancer in the chromate industry: a quantitative risk assessment, Risk Anal. 24 (2004) 1099–1108, https://doi.org/10.1111/j.0272-4332.2004.00512.x.
[21] L. Girelli, M. Tocci, M. Conte, R. Giovanardi, P. Veronesi, M. Gelfi, A. Pola, Effect of the T6 heat treatment on corrosion behavior of additive manufactured and gravity cast AlSi10Mg alloy, Mater. Corros. 70 (2019) 1808–1816, https://doi.org/10.1002/maco.201910890.
[22] R.I. Revilla, D. Verkens, T. Rubben, I. de Graeve, Corrosion and corrosion protection of additively manufactured Aluminium alloys-a critical review, Materials (Basel) 13 (2020), https://doi.org/10.3390/ma13214804.
[23] P. Jantimapornkij, J. Zerrer, A. Buling, Advanced corrosion protection of additive manufactured light metals by creating ceramic SurfaceThrough CERANOD® plasma Electrolytical oxidation process, Front. Chem. Eng. 3 (2021) 734644, https://doi.org/10.3389/fceng.2021.734644.
[24] R.O. Hussein, D.O. Northwood, X. Nie, The effect of processing parameters and substrate composition on the corrosion resistance of plasma electrolytic oxidation (PEO) coated magnesium alloys, Surf. Coat. Technol. 237 (2013) 357–368, https://doi.org/10.1016/j.surfcoat.2013.09.021.
[25] X. Huang, Plasma electrolytic oxidation coatings on aluminum alloys: microstructures, properties, and applications, MCMS 2 (2019). doi:10.33552/MCMS.2019.02.000526.
[26] L. Macera, D. Pullini, A. Boschetto, L. Bottini, C. Mingazzini, G.L. Falleti, Sol–Gel Silica Coatings for Corrosion Protection of Aluminum Parts Manufactured by Selective Laser Melting (SLM) Technology, Coatings 13 (2023) 1081. doi: https://doi.org/10.3390/coatings13061081.
[27] M.L. Zheludkevich, R. Serra, M.F. Montemor, I.M. Salvado, M. Ferreira, Corrosion protective properties of nanostructured sol–gel hybrid coatings to AA2024-T3, Surf. Coat. Technol. 200 (2006) 3084–3094, https://doi.org/10.1016/j.surfcoat.2004.09.007.
[28] Y. Liu, D. Sun, H. You, J.S. Chung, Corrosion resistance properties of organic–inorganic hybrid coatings on 2024 aluminum alloy, Appl. Surf. Sci. 246 (2005) 82–89. doi:https://doi.org/10.1016/j.apsusc.2004.10.040.
[29] Mandakini N. Chaudhari, Thin film deposition methods: a critical review, Int. J. Res. Appl. Sci. Eng. Technol. 9 (2021) 5215–5232.
[30] Z. Zhou, C. Li, R. Wang, H. Tao, D. Yang, S. Qin, X. Meng, C. Zhou, Crosslinking control of hydrophobic benzoxazine-based hybrid sol-gel coating for corrosion protection on aluminum alloys, Prog. Org. Coat. 171 (2022) 107059, https://doi.org/10.1016/j.porgcoat.2022.107059.
[31] L. Li, J. He, J. Lei, W. Xu, X. Jing, X. Ou, S. Wu, N. Li, S. Zhang, A sol–bath–gel approach to prepare hybrid coating for corrosion protection of aluminum alloy, Surf. Coat. Technol. 279 (2015) 72–78, https://doi.org/10.1016/j.surfcoat.2015.08.032.
[32] Y. Jafari-Tarzanagh, D. Seifzadeh, A. Khodayari, R. Samadianfard, Active corrosion protection of AA2024 aluminum alloy by sol-gel coating containing inhibitor-

loaded mesoporous SBA-15, Prog. Org. Coat. 173 (2022) 107166, https://doi.org/10.1016/j.porgcoat.2022.107166.
[33] U. Lommatzsch, J. Ihde, Plasma polymerization of HMDSO with an atmospheric pressure plasma jet for corrosion protection of aluminum and low-adhesion surfaces, Plasma Process. Polym. 6 (2009) 642–648, https://doi.org/10.1002/ppap.200900032.
[34] V. Hopfe, D.W. Sheel, Atmospheric-pressure plasmas for wide-area thin-film deposition and etching, Plasma Process. Polym. 4 (2007) 253–265, https://doi.org/10.1002/ppap.200600202.
[35] C. Regula, J. Ihde, U. Lommatzsch, R. Wilken, Corrosion protection of copper surfaces by an atmospheric pressure plasma jet treatment, Surf. Coat. Technol. 205 (2011) S355–S358, https://doi.org/10.1016/j.surfcoat.2011.03.126.
[36] F. Fanelli, F. Fracassi, Atmospheric pressure non-equilibrium plasma jet technology: general features, specificities and applications in surface processing of materials, Surf. Coat. Technol. 322 (2017) 174–201, https://doi.org/10.1016/j.surfcoat.2017.05.027.
[37] D. Merche, N. Vandencasteele, F. Reniers, Atmospheric plasmas for thin film deposition: a critical review, Thin Solid Films 520 (2012) 4219–4236, https://doi.org/10.1016/j.tsf.2012.01.026.
[38] R. Thyen, A. Weber, C.-P. Klages, Plasma-enhanced chemical-vapour-deposition of thin films by corona discharge at atmospheric pressure, Surf. Coat. Technol. 97 (1997) 426–434, https://doi.org/10.1016/S0257-8972(97)00158-8.
[39] F. Massines, C. Sarra-Bournet, F. Fanelli, N. Naudé, N. Gherardi, Atmospheric pressure low temperature direct plasma technology: status and challenges for thin film deposition, Plasma Process. Polym. 9 (2012) 1041–1073, https://doi.org/10.1002/ppap.201200029.
[40] E. Vassallo, A. Cremona, L. Laguardia, E. Mesto, Preparation of plasma-polymerized SiOx-like thin films from a mixture of hexamethyldisiloxane and oxygen to improve the corrosion behaviour, Surf. Coat. Technol. 200 (2006) 3035–3040, https://doi.org/10.1016/j.surfcoat.2004.11.001.
[41] B.J. Jones, L. Anguilano, J.J. Ojeda, Argon plasma treatment techniques on steel and effects on diamond-like carbon structure and delamination, Diam. Relat. Mater. 20 (2011) 1030–1035, https://doi.org/10.1016/j.diamond.2011.06.004.
[42] Y.-Y. Ji, Y.-C. Hong, S.-H. Lee, S.-D. Kim, S.-S. Kim, Formation of super-hydrophobic and water-repellency surface with hexamethyldisiloxane (HMDSO) coating on polyethyleneteraphtalate fiber by atmosperic pressure plasma polymerization, Surf. Coat. Technol. 202 (2008) 5663–5667, https://doi.org/10.1016/j.surfcoat.2008.06.151.
[43] Lucia Bonova, Anna Zahoranova, Dusan Kovacik, Deposition of polymer films on aluminium surface using atmospheric-pressure plasma, Chem. List. 106 (2012) 1431–1434.
[44] Y. Zhou, Plasma polymerized coatings for improved corrosion resistance: PhD thesis.
[45] M. Dabalà, L. Armelao, A. Buchberger, I. Calliari, Cerium-based conversion layers on aluminum alloys, Appl. Surf. Sci. 172 (2001) 312–322, https://doi.org/10.1016/S0169-4332(00)00873-4.
[46] P. Rodič, I. Milošev, M. Lekka, F. Andreatta, L. Fedrizzi, Study of the synergistic effect of cerium acetate and sodium sulphate on the corrosion inhibition of AA2024-T3, Electrochim. Acta 308 (2019) 337–349, https://doi.org/10.1016/j.electacta.2019.04.042.
[47] P. Rodič, M. Lekka, F. Andreatta, I. Milošev, L. Fedrizzi, The synergistic effect of cerium acetate and sodium sulphate on corrosion inhibition of AA2024-T3 at various temperatures, Electrochim. Acta 370 (2021) 137664, https://doi.org/10.1016/j.electacta.2020.137664.
[48] P. Rodič, I. Milošev, G.S. Frankel, Corrosion of synthetic intermetallic compounds and AA7075-T6 in dilute Harrison's solution and inhibition by cerium(III) salts, J. Electrochem. Soc. 170 (2023) 31503, https://doi.org/10.1149/1945-7111/acc0a3.
[49] A.J. Aldykewicz, H.S. Isaacs, A.J. Davenport, The investigation of cerium as a cathodic inhibitor for aluminum-copper alloys, J. Electrochem. Soc. 142 (1995) 3342–3350, https://doi.org/10.1149/1.2049985.
[50] T.G. Harvey, Cerium-based conversion coatings on aluminium alloys: a process review, Corros. Eng. Sci. Technol. 48 (2013) 248–269, https://doi.org/10.1179/1743278213Y.0000000089.
[51] P. Rodič, I. Milošev, The influence of additional salts on corrosion inhibition by cerium(III) acetate in the protection of AA7075-T6 in chloride solution, Corros. Sci. 149 (2019) 108–122, https://doi.org/10.1016/j.corsci.2018.10.021.
[52] I. Milosev, P. Rodic, Cerium chloride and acetate salts as corrosion inhibitors for aluminium alloy AA7075-T6 in sodium chloride solution, Corrosion (2016), https://doi.org/10.5006/1956.
[53] S.V. Harb, A. Trentin, T.A.C. de Souza, M. Magnani, S.H. Pulcinelli, C.V. Santilli, P. Hammer, Effective corrosion protection by eco-friendly self-healing PMMA-cerium oxide coatings, Chem. Eng. J. 383 (2020) 123219, https://doi.org/10.1016/j.cej.2019.123219.
[54] N.C. Rosero-Navarro, L. Paussa, F. Andreatta, Y. Castro, A. Durán, M. Aparicio, L. Fedrizzi, Optimization of hybrid sol–gel coatings by combination of layers with complementary properties for corrosion protection of AA2024, Prog. Org. Coat. 69 (2010) 167–174, https://doi.org/10.1016/j.porgcoat.2010.04.013.
[55] K. Aramaki, Improvement in the self-healing ability of a protective film consisting of hydrated cerium(III) oxide and sodium phosphate layers on zinc, Corros. Sci. 45 (2003) 451–464, https://doi.org/10.1016/S0010-938X(02)00122-1.
[56] N. Mubarak, J. Hu, S. Tang, Electrochemical study of unmodified and inhibitor doped Silane films for corrosion protection of AA2024-T3, IOP Confer. Ser. Mater. Sci. Eng. 230 (2017) 12045, https://doi.org/10.1088/1757-899X/230/1/012045.
[57] E. González, R. Stuhr, J.M. Vega, E. García-Lecina, H.-J. Grande, J.R. Leiza, M. Paulis, Assessing the effect of CeO2 nanoparticles as corrosion inhibitor in hybrid biobased waterborne acrylic direct to metal coating binders, Polymers (Basel) 13 (2021), https://doi.org/10.3390/polym13060848.
[58] O.V. Penkov, M. Khadem, W.-S. Lim, D.-E. Kim, A review of recent applications of atmospheric pressure plasma jets for materials processing, J. Coat. Technol. Res. 12 (2015) 225–235, https://doi.org/10.1007/s11998-014-9638-z.
[59] L. Soukup, Z. Hubička, A. Churpita, M. Čada, P. Pokorný, J. Zemek, K. Jurek, L. Jastrabík, Investigation of the atmospheric RF torch-barrier plasma jet for deposition of CeOx thin films, Surf. Coat. Technol. 169-170 (2003) 571–574. doi: https://doi.org/10.1016/S0257-8972(03)00097-5.
[60] D. Patel, L. Bonova, Z. Jeckell, D.E. Barlaz, S. Chaudhuri, D.V. Krogstad, D. N. Ruzic, Deposition of zirconium oxide using atmospheric pressure plasma enhanced chemical vapor deposition with various precursors, Thin Solid Films 733 (2021) 138815, https://doi.org/10.1016/j.tsf.2021.138815.
[61] ASTM, International, Standard Test Method for Determining Volume Fraction by Systematic Manual Point Count, https://www.astm.org/e0562-02.html, 2025. (Accessed 6 March 2025).
[62] P. Uznanski, A. Walkiewicz-Pietrzykowska, K. Jankowski, J. Zakrzewska, A. M. Wrobel, J. Balcerzak, J. Tyczkowski, Atomic hydrogen induced chemical vapor deposition of silicon Oxycarbide thin films derived from Diethoxymethylsilane precursor, Appl. Orga. Chem. 34 (2020) e5674, https://doi.org/10.1002/aoc.5674.
[63] H. Shimizu, S. Nagano, A. Uedono, N. Tajima, T. Momose, Y. Shimogaki, Material design of plasma-enhanced chemical vapour deposition SiCH films for low-k cap layers in the further scaling of ultra-large-scale integrated devices-cu interconnects, Sci. Technol. Adv. Mater. 14 (2013) 55005, https://doi.org/10.1088/1468-6996/14/5/055005.
[64] D. Hegemann, U. Vohrer, C. Oehr, R. Riedel, Deposition of SiOx films from O2/HMDSO plasmas, Surf. Coat. Technol. 116-119 (1999) 1033–1036, https://doi.org/10.1016/S0257-8972(99)00092-4.
[65] P. Rodič, J. Katić, D. Korte, P. Desimone, M. Franko, S. Ceré, M. Metikoš-Huković, I. Milošev, The effect of cerium ions on the structure, Porosity and Electrochemical Properties of Si/Zr-Based Hybrid Sol-Gel Coatings Deposited on Aluminum, Metals 8 (2018) 248, https://doi.org/10.3390/met8040248.
[66] Z. Ahmad, Chapter 7 - coatings, in: Z. Ahmad (Ed.), Principles of Corrosion Engineering and Corrosion Control, Butterworth-Heinemann, Oxford, 2006, pp. 382–437.
[67] Aluminum Anodizing Reference Guide | AAC, 2024. https://www.anodizing.org/page/anodizing-reference-guide (accessed 3 December 2024).
[68] Elsevier Science (Ed.), Shreir's Corrosion. Volume 4, Management and control of corrosion: 4.38 - Management of Corrosion of Aircraft, 2009.
[69] W. Möller, M. Schmidt, Untersuchungen zur chemischen Struktur von Glimmpolymerschichten aus Hexamethyldisiloxan (HMDS), Contrib, Plasma Phys. 17 (1977) 121–134, https://doi.org/10.1002/ctpp.19770170206.
[70] A. Grill, D.A. Neumayer, Structure of low dielectric constant to extreme low dielectric constant SiCOH films: Fourier transform infrared spectroscopy characterization, J. Appl. Phys. 94 (2003) 6697–6707, https://doi.org/10.1063/1.1618358.
[71] G. Wulf, B. Mayer, U. Lommatzsch, Plasma co-polymerization of HMDSO and limonene with an atmospheric pressure plasma jet, Plasma 5 (2022) 44–59, https://doi.org/10.3390/plasma5010004.
[72] N.M. Santos, T.M. Gonçalves, J. de Amorim, C.M. Freire, J.R. Bortoleto, S. F. Durrant, R.P. Ribeiro, N.C. Cruz, E.C. Rangel, Effect of the plasma excitation power on the properties of SiOxCyHz films deposited on AISI 304 steel, Surf. Coat. Technol. 311 (2017) 127–137, https://doi.org/10.1016/j.surfcoat.2016.12.113.
[73] W. Wirth, J. Comeaux, S. Jang, Characterization of flexible low-dielectric constant carbon-doped oxide (SiCOH) thin films under repeated mechanical bending stress, J. Mater. Sci. 57 (2022) 21411–21431, https://doi.org/10.1007/s10853-022-07987-y.
[74] T.R. Gengenbach, H.J. Griesser, Post-deposition ageing reactions differ markedly between plasma polymers deposited from siloxane and silazane monomers, Polymer 40 (1999) 5079–5094, https://doi.org/10.1016/S0032-3861(98)00727-7.
[75] J.V. Gordon, S.P. Narra, R.W. Cunningham, H. Liu, H. Chen, R.M. Suter, J.L. Beuth, A.D. Rollett, Defect structure process maps for laser powder bed fusion additive manufacturing, Addit. Manuf. 36 (2020) 101552, https://doi.org/10.1016/j.addma.2020.101552.
[76] R. Zamiri, H.A. Ahangar, A. Kaushal, A. Zakaria, G. Zamiri, D. Tobaldi, J.M. F. Ferreira, Dielectrical properties of CeO2 nanoparticles at different temperatures, PLoS One 10 (2015) e0122989, https://doi.org/10.1371/journal.pone.0122989.
[77] F. Schwabe, R. Schulin, P. Rupper, A. Rotzetter, W. Stark, B. Nowack, Dissolution and transformation of cerium oxide nanoparticles in plant growth media, J. Nanopart. Res. 16 (2014), https://doi.org/10.1007/s11051-014-2668-8.
[78] C. Ma, J. Fu, J. Chen, Y. Wen, P.O. Fasan, H. Zhang, N. Zhang, J. Zheng, B.-H. Chen, Improving the surface properties of CeO 2 by dissolution of Ce 3+ to enhance the performance for catalytic wet air oxidation of phenol, Ind. Eng. Chem. Res. 56 (2017) 9090–9097, https://doi.org/10.1021/acs.iecr.7b02121.
[79] J. Shang, F. Liu, G. Gu, L. Meng, Effects of Ce(NO 3) 3 concentration on microstructure and properties of plasma electrolytic oxidation layer on 6061 alloy, Mater. Res. Express 9 (2022) 96513. doi:https://doi.org/10.1088/2053-1591/ac859f.
[80] A. Stancampiano, T. Gallingani, M. Gherardi, Z. Machala, P. Maguire, V. Colombo, J.-M. Pouvesle, E. Robert, Plasma and aerosols: challenges, opportunities and perspectives, Appl. Sci. 9 (2019) 3861, https://doi.org/10.3390/app9183861.